

POLITECNICO DI TORINO

Corso di Laurea Magistrale
in Ingegneria Aerospaziale



Tesi di Laurea Magistrale

Numerical simulations of reacting flows in innovative combustors

Relatore

Prof. Michele FERLAUTO

Candidato

Salvatore MANGANARO

Aprile 2021

Abstract

New laws and regulations issued to reduce environmental impact and interests in supersonic engines impose the development of newer combustor geometries and it is fundamental analyze their functioning first of all with numerical simulations. This work aims to study the behavior of different combustor geometries with main focus on innovative configurations and non pre-mixed combustion. Numerical simulations of reacting flows in classical and advanced combustor geometries have been performed. Different conditions have been tested in terms of numerical setups and reaction mechanisms such as use of CH_4 and H_2 as fuel with air mixture (O_2 and N_2) for the methane and LOX for gaseous hydrogen. As classical geometry, the "Penn State pre-burner" has been chosen while a trapped-vortex style combustor has been selected as advanced geometry. Alternative results for temperature distribution and reaction products of these various applications are shown and discussed. For the trapped-vortex combustor, further investigations involving combustion efficiency (presence of unburnt fuel) have been conducted.

"e quindi uscimmo a riveder le stelle."
(Inferno XXXIV, 139)

A Padre Samuele

Table of Contents

List of Figures	VI
Introduction	1
1 Modeling the physical phenomenon	4
1.1 Navier-Stokes equations	4
1.1.1 Conservation of mass	6
1.1.2 Conservation of momentum	6
1.1.3 Conservation of energy	7
1.1.4 Navier-Stokes closure	8
1.2 Equations for reacting flows	9
1.2.1 State Equation	9
1.2.2 Thermal radiation	10
1.2.3 Chemical reactions	11
1.2.4 Conservation of mass fraction	14
1.2.5 High temperature effects	16
1.3 Turbulence	17
1.3.1 Reynolds-Averaged Navier-Stokes (RANS)	19
1.3.2 Standard k - ϵ model	20
1.3.3 k - ω Shear Stress Transport Model	21
1.3.4 Reynolds Stress Transport Models	22
1.3.5 Large Eddy Simulations (LES)	22
1.3.6 Smagorinsky-Lilly Model	22
1.3.7 One Equation Model	23
1.4 Turbulent combustion	23
1.4.1 Eddy dissipation concept (EDC)	25
1.4.2 Partially stirred reactor (PaSR)	26
1.5 Summary	27

2	Computational Fluid-Dynamics (CFD)	29
2.1	Numerical methods	29
2.1.1	Finite Difference Method	32
2.1.2	Finite Volume Method	37
2.2	Explicit and implicit numerical schemes and their properties	39
2.2.1	Convergence	41
2.2.2	Stability	41
2.2.3	Lower limit for Courant number	45
2.3	Summary	46
3	Test cases description	48
3.1	Advanced Vortex Combustor (AVC)	49
3.1.1	Geometry	50
3.1.2	Numerical setup	50
3.1.3	Initial and boundary conditions	52
3.2	Penn State pre-burner	53
3.2.1	Geometry	53
3.2.2	Numerical setup	54
3.2.3	Initial and boundary conditions	55
4	Results	57
4.1	AVC	57
4.1.1	Fluid-dynamic	57
4.1.2	Temperature distribution	59
4.1.3	CO ₂ distribution	61
4.1.4	CH ₄ distribution and combustion efficiency	63
4.2	Penn State pre-burner	66
4.2.1	Fluid-dynamic	67
4.2.2	Temperature distribution	68
4.2.3	H ₂ O, N ₂ , and O ₂ distribution	70
4.2.4	H ₂ distribution	72
5	Conclusions	75
	Appendices	77
A	AVC	78
A.1	GMSH	78
A.2	openFOAM	81
A.2.1	chemistryProperties	81
A.2.2	combustionProperties	83
A.2.3	reactions	83

A.2.4	thermo.compressibleGAS	84
A.2.5	thermohysicalProperties	87
A.2.6	controlDict	87
A.2.7	fvSchemes	88
A.2.8	fvSolution	89
B	Penn State pre-burner	92
B.1	GMSH	92
B.2	openFOAM	96
B.3	Chamber wall temperature distribution script	96
B.3.1	chemistryProperties	96
B.3.2	combustionProperties	98
B.3.3	reactions	98
B.3.4	thermo.compressibleGAS	99
B.3.5	thermohysicalProperties	101
B.3.6	turbulenceProperties	101
B.3.7	controlDict	102
B.3.8	fvSchemes	103
B.3.9	fvSolution	104
B.3.10	setFieldsDict	105
	Bibliography	107

List of Figures

1.1	Control volume	5
1.2	Thermal radiation hitting a body.	12
1.3	Dof for a triatomic molecule	17
1.4	Activation of degrees of freedom (dof)	17
1.5	Fine structure [4]	25
1.6	Trade between accuracy and computational cost [4]	26
2.1	u function of x	33
2.2	Slope difference in approximation methods	34
2.3	Problem capturing boundaries with constant grid	35
2.4	Variable intervals	36
2.5	Control volume divided in three sub-volumes	37
2.6	Focus on a 2D cell	38
2.7	Example of generic periodic distribution in x of the round-off error	42
2.8	Different characteristic lines	45
3.1	Geometric details for the fuel inlet and the second blunt body [6].	50
3.2	PIMPLE algorithm flow-chart [7]	51
3.3	Mesh generated with GMSH for the AVC geometry	52
3.4	Detail of first cavity from the AVC mesh	52
3.5	Detailed schematic of pre-combustor[8].	53
3.6	Detail of Penn State injector[8].	54
3.7	Detail of computational mesh near the injector exit	55
3.8	Penn State initial conditions	56
4.1	Detail of streamlines inside the cavity	58
4.2	Eddies evolution through time for $U_a = 50 \text{ m/s}$	58
4.3	Outlet velocity profile	59
4.4	Temperature profiles for $U_a = 50 \text{ m/s}$ (top) and $U = 100 \text{ m/s}$ (bottom)	59
4.5	Temperature profiles for $U_a = 75 \text{ m/s}$ (top) and $U_a = 25 \text{ m/s}$ (bottom)	60

4.6	Outlet temperature profile	61
4.7	Comparison of CO ₂ distribution and H ₂ O distribution for $U_a = 50 \text{ m/s}$	62
4.8	CO ₂ distribution for $U_a = 50 \text{ m/s}$ (top) and $U = 100 \text{ m/s}$ (bottom)	62
4.9	CO ₂ distribution for $U_a = 75 \text{ m/s}$ (top) and $U = 25 \text{ m/s}$ (bottom)	63
4.10	Outlet CO ₂ mass fraction profile	63
4.11	CH ₄ distribution for $U_a = 50 \text{ m/s}$ (top) and $U = 100 \text{ m/s}$ (bottom)	64
4.12	CH ₄ distribution for $U_a = 75 \text{ m/s}$ (top) and $U = 25 \text{ m/s}$ (bottom)	64
4.13	Efficiency trend with respect to air inlet velocity	65
4.14	Efficiency trend with respect to air inlet velocity	66
4.15	Streamlines highlighting outer eddie and main flow direction	67
4.16	Streamlines highlighting eddies inside the chamber	68
4.17	Mach number at the chamber inlet	68
4.18	Mach number along the outlet nozzle	69
4.19	Measurements along the symmetry axis inside the outlet nozzle	69
4.20	Temperature profile	70
4.21	Temperature measurements for a cross section at $z = 0.285 \text{ m}$	70
4.22	H ₂ O distribution in the chamber	71
4.23	N ₂ distribution inside the chamber	71
4.24	O ₂ distribution inside the chamber	72
4.25	H ₂ O, N ₂ , and O ₂ mass fraction measurements for a cross section at $z = 0.285 \text{ m}$	73
4.26	H ₂ O distribution in the chamber	73
4.27	H ₂ mass fraction measurements for a cross section put at $z = 0.285 \text{ m}$	74

Introduction

Climate change emergency has touched mostly every economic fields, from first necessity goods manufacturing to transport. In order to respond to this global crisis, government, organizations and agencies have imposed limits on emissions, especially those involving greenhouse gasses and NO_x .

These limitations have had huge impact on the aerospace way of thinking: from the design of new components, all the way to whole spacecrafts and aircraft's design, every thing comes down to respect the requirements set by laws. While for other industrial fields, these "green laws" may disagree with economical advantages, they go hand to hand with airway companies desire to reduce fuel consumption which inevitably leads to fewer costs.

Europe first move to actively stop climate change was "*A Vision for 2020*" which was a set of objectives to reach before 2020. Those goals not only were about chemical pollution such as gas emissions but they also included noise pollution. [1] Together with points concerning safety, security, and competitiveness, this document established the creation of the *Advisory Council for Aeronautical Research in Europe* (ACARE) formed by members from main aeronautical companies. This council set environmental targets which ideally where concerning not only the engine but the whole aircraft. Said objectives were:

- Reduce perceived external noise by 50% (30dB cumulative);
- Reduce NO_x emissions by 80%;
- Reduce Fuel consumption and CO_2 emissions by 50%.

To satisfy what European governments were asking, since the main reason for chemical and acoustic pollution is without any doubt the engine, aerospace industry immediately focused its energies and resources into developing new concept for it. ACARE standards were very difficult to reach by the end of 2020 and that led to a failure of *Vision for 2020*, in fact, in 2011, ACARE set a new deadline and with it, new objectives in what it is called *Flightpath 2050*[2]. This time, the bar was set even higher than done previously in *vision for 2020*:

- 75% reduction in CO_2 per passenger kilometre;

-
- 90% reduction in NO_x emissions;
 - 65% reduction in noise.¹

In order to achieve these goals, it is not enough just to reinvent the engine but the whole aircraft design needs to be revolutionized.

Concerning the engine, to cope with those very difficult requests, a lot of innovative and futuristic designs have been proposed: from taking to the limits classic concepts (ultra high bypass engine and open rotor), to modify its basic architecture revisiting its thermodynamic core and components. One concept that stands out from the rest is *adaptable engines* or *switch mode engines*. As their name suggest, these engines are designed to give the best results in terms of consumption and emissions in different working conditions. This can be achieved basically in two different ways: change in fuel (e.g. from fossil fuel to liquid hydrogen and vice versa), or change in geometry. Whether a change in fuel or in geometry is employed, one element of the engine seems to be mostly effected i.e. the combustor.

Designing and adaptable combustor is a very difficult challenge for a slight change in its geometry may lead to increase in NO_x, CO₂, unburnt fuel emissions, and in some cases, to combustion instability and flame blow out.

Besides switch-mode combustors, research is focusing on new designs to improve combustion efficiency and emissions. One concept that is frequently cited in articles and papers is the *Advanced Vortex Combustor*(AVC), often referred to as *Trapped Vortex Combustor* even though they are not quite the same thing. These kinds of combustor rely mostly on cavities to trap eddies (as the name suggests) in order to obtain the right amount of time to achieve the most efficient combustion possible. In addition to that, the vortexes suck in fresh air (or any other oxidizer used) to control the temperature cooling down the products and so stopping the formation of NO_x. Dan Zhao et al. in [3] have done a great work in resuming the evolution and characteristics of these very actual combustors.

Just like every thing in modern aviation, a multidisciplinary analysis is needed to study at their best new combustion concepts. That is where computational fluid-dynamic (CFD) has a big role. CFD is a very useful tool and a very economic one with respect to actual physical experimentation. It is often used to obtain first results in preliminary drafts that may be perfected further in the design process. The goal of this work is to use CFD simulation to get some results that may describe in first approximation how some innovative concepts for combustors behaves, their capabilities and advantages in terms of combustion efficiency (un-burnt fuel) and pollutant emissions for non pre-mixed reactants. As a secondary matter, it is interesting to analyze how certain high velocities affect the combustion process and

¹Both vision 2020 and flightpath 2050 targets are compared to 2000 data

establish whether or not these designs may be suited for high Mach flights (RAM jet or even SCRAM jet).

There are numerous CFD software to choose from, the one used in this study is OpenFOAM². OpenFOAM is an open-source software which makes it very adaptable for any kind of scenario one may study. Having the possibility to look inside its code allows the user to change it in a way that makes it ad hoc for each study-case and that is a very important quality to have especially for any research and academic purposes. The reactingFOAM solver is the most suited one to use since it is the most generic one for combustions and works perfectly fine with non pre-mixed flows as those of the test cases analyzed in this work.

Concerning the structure of this document, it is organized as follows:

- Chapter 1 introduces and describes all those equations and mathematical relations needed in order to describe the physical phenomenon of combustion;
- Chapter 2 explains the logic behind Computational Fluid-Dynamics, its essentials theories and methods;
- Chapter 3 describes the test cases behind this work: their geometries, computational mesh, initial and boundary conditions, and numerical setup as well as reaction mechanisms;
- Chapter 4 shows results obtained from numerical simulations using reacting-FOAM with the help of images and plots;
- Chapter 5 is dedicated to conclusive observations that may be extrapolated from the results.

²Open source Field Operation And Manipulation

Chapter 1

Modeling the physical phenomenon

1.1 Navier-Stokes equations

The behavior of a fluid, whether it is a liquid or a gas, can be described through simple natural laws which are translated into mathematical language with very complicated equations, those are the conservation of mass, momentum and energy. Before writing the equations, it is necessary to clarify the two different approaches or point of views used to study fluids: Lagrangian and Eulerian point of view.

According to the Eulerian method, the fluid flow is studied inside an arbitrary fixed volume called *control volume*. Inside that volume, elementary quantities are function of space and time e.g. $\mathbf{q} = \mathbf{q}(x, y, z, t)$, $T = T(x, y, z, t)$. Using Euler's point of view, one obtains the *integral* or *conservative form*.

In the Lagrangian point of view, the change in elementary quantities is analyzed along the trajectory of a fluid particle which is described as an infinitesimal volume big enough that the continuum hypotheses are satisfied. The equations of motion written with this method are called *non-conservative*. Usually, when handling the equations in this form, a new mathematical operator needs to be introduced: *the total derivative* also known as *material*, *Lagrangian*, or *substantial*.

$$\frac{D(\cdot)}{Dt} = \frac{\partial(\cdot)}{\partial t} + \mathbf{q} \cdot \nabla(\cdot) \quad (1.1)$$

Just like the Lagrangian method, the material derivative follows the fluid particle variation along its trajectory. $\partial(\cdot)/\partial t$ is called *local derivative* and it studies the local variation at a fixed point. The particles which go through that certain point will have different values of pressure, velocity and so on. $\mathbf{q} \cdot \nabla(\cdot)$ is called *convective derivative*, it still represents a variation in time but it analyzes the changing in the

motion of the particle.

Mathematically speaking, both forms are identical, one can choose either one of them and they would describe the same phenomenon, although in some case it is more reasonable to use the Lagrangian form and vice-versa. This concept cannot be applied in *computational fluid dynamics (CFD)* where using one type of equation may introduce numerical errors avoidable with the other form.

In order to introduce the concept of reacting flows gradually, first, every chemical source of any sort is neglected and will be taken account in next section.

All three conservation equations have the same structure: the variation in time of the quantity is equal to its flux and possible sources.

$$\frac{d(\cdot)}{dt} = \Phi(\cdot) + \text{sources} \quad (1.2)$$

The Eulerian point of view is used to derive the final form of the equations. Before

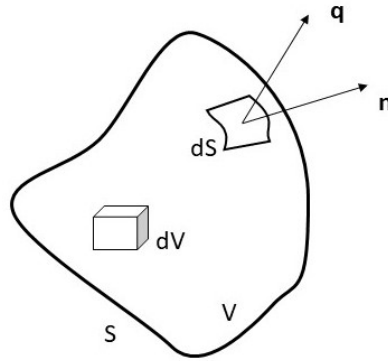


Figure 1.1: Control volume

digging relatively deep into the equations, it is important to state that there are mainly three type of flows: *incompressible*, *weakly compressible*, and *compressible*. In incompressible flows, the density is constant which leads to equation (1.7). This type of flow can be solved by using just the conservation of mass and the conservation of momentum. In weakly compressible flows, the density may change but mainly because of a variation in temperature which can occur following a chemical reaction which keeps the pressure nearly constant. The solution still requires the conservation of energy in order to find the temperature. Compressible flows are clearly the opposite of incompressible flows which means the assuming $\rho = \text{const}$ is a mistake. Solving this flow requires the conservation of energy and the state equation which is the link between the continuity equation and the momentum equation.

1.1.1 Conservation of mass

Let ρ be the density of the fluid inside the control volume, then

$$\frac{d}{dt} \int_V \rho dV + \int_S \rho \mathbf{q} \cdot \mathbf{n} dS = 0 \quad (1.3)$$

represents the integral form of conservation of mass where $\mathbf{q} = u\hat{i} + v\hat{j} + w\hat{k}$ is the velocity thus $\int_S \rho \mathbf{q} \cdot \mathbf{n} dS$ is the flux through the surface of the control volume. Since eventual chemical reactions are neglected, there is no source. Knowing that the control volume does not depend on time and using Gauss theorem, equation (1.3) leads to

$$\frac{\partial \rho}{\partial t} + \nabla \cdot (\rho \mathbf{q}) = 0 \quad (1.4)$$

which is the differential conservative form also known as *continuity equation*. Because

$$\nabla \cdot (\rho \mathbf{q}) = \frac{\partial(\rho u)}{\partial x} + \frac{\partial(\rho v)}{\partial y} + \frac{\partial(\rho w)}{\partial z} \quad (1.5)$$

the equation (1.4) can be written as

$$\frac{D\rho}{Dt} + \rho \nabla \cdot \mathbf{q} = 0. \quad (1.6)$$

From eq. (1.6) it can be easily deduced that if $\rho = \text{const}$ then

$$\nabla \cdot \mathbf{q} = 0 \quad (1.7)$$

which is the continuity equation for *incompressible flow*.

1.1.2 Conservation of momentum

The mass momentum associated with an infinitesimal volume dV is $\rho \mathbf{q}$, thus

$$\frac{d}{dt} \int_V \rho \mathbf{q} dV + \int_S \rho \mathbf{q} \mathbf{q} dS = \int_S \bar{\boldsymbol{\sigma}} \cdot \mathbf{n} dS + \int_V \rho \mathbf{f} dV. \quad (1.8)$$

is the integral form for the conservation of momentum. \mathbf{f} gathers any external force per unit volume (gravity, electromagnetic field...) while $\bar{\boldsymbol{\sigma}}$ represents the *stress tensor*

$$\bar{\boldsymbol{\sigma}} = -p\bar{\mathbf{I}} + \bar{\boldsymbol{\tau}} \quad (1.9)$$

where p (pressure) is normal to the surface and $\bar{\boldsymbol{\tau}}$ (viscosity strain) is tangential to the surface and it is a symmetrical 6×6 tensor and $\bar{\mathbf{I}}$ is the *Identity matrix*.

$$\bar{\boldsymbol{\tau}} = \begin{Bmatrix} \tau_{xx} & \tau_{xy} & \tau_{xz} \\ \tau_{xy} & \tau_{yy} & \tau_{yz} \\ \tau_{xz} & \tau_{yz} & \tau_{zz} \end{Bmatrix}; \quad \bar{\mathbf{I}} = \begin{Bmatrix} 1 & 0 & 0 \\ 0 & 1 & 0 \\ 0 & 0 & 1 \end{Bmatrix}. \quad (1.10)$$

The conservative form of equation (1.8) is

$$\frac{\partial(\rho\mathbf{q})}{\partial t} + \nabla \cdot (\rho\mathbf{q}\mathbf{q}) = -\nabla p + \nabla \cdot \bar{\boldsymbol{\tau}} + \rho\mathbf{f} \quad (1.11)$$

Re-writing equation (1.11) and adding the continuity equation multiplied by \mathbf{q} leads to

$$\rho \frac{D\mathbf{q}}{Dt} = -\nabla p + \nabla \cdot \bar{\boldsymbol{\tau}} + \rho\mathbf{f} \quad (1.12)$$

which is the equivalent of $\mathbf{F} = m\mathbf{a}$, in fact, while the conservation of mass is a scalar equation, the conservation of momentum is a vectorial relation i.e. it includes three different equations: one for x-direction, one for the y-direction and one for the z-direction (if expressed in Cartesian coordinates).

$$\begin{cases} \rho \left(\frac{\partial u}{\partial t} + u \frac{\partial u}{\partial x} + v \frac{\partial u}{\partial y} + w \frac{\partial u}{\partial z} \right) = -\frac{\partial p}{\partial x} + \nabla \cdot \boldsymbol{\tau}_x + \rho f_x \\ \rho \left(\frac{\partial v}{\partial t} + u \frac{\partial v}{\partial x} + v \frac{\partial v}{\partial y} + w \frac{\partial v}{\partial z} \right) = -\frac{\partial p}{\partial y} + \nabla \cdot \boldsymbol{\tau}_y + \rho f_y \\ \rho \left(\frac{\partial w}{\partial t} + u \frac{\partial w}{\partial x} + v \frac{\partial w}{\partial y} + w \frac{\partial w}{\partial z} \right) = -\frac{\partial p}{\partial z} + \nabla \cdot \boldsymbol{\tau}_z + \rho f_z \end{cases} \quad (1.13)$$

Under the hypotheses of a Newtonian fluid, it is possible to write

$$\tau_{ij} = \mu \left(\frac{\partial u_i}{\partial x_j} + \frac{\partial u_j}{\partial x_i} \right) - \frac{2}{3} \mu \nabla \cdot \mathbf{q} \delta_{ij} \quad (1.14)$$

with

$$\delta_{ij} = \begin{cases} 1 & i = j \\ 0 & i \neq j \end{cases} \quad (1.15)$$

Historically the conservation of momentum and the equation of continuity are called *Navier-Stokes equation* while fluid-dynamically they also include the conservation of energy.

1.1.3 Conservation of energy

Usually the only forms of energy that are considered while speaking of gases are the kinetic energy and the internal energy thus

$$E = e + \frac{q^2}{2} \quad (1.16)$$

is the energy per unit mass associated with a volume dV . The integral form of the conservation of energy is

$$\int_V \rho E dV + \int_S \rho E \mathbf{q} \cdot \mathbf{n} = - \int_S p \mathbf{q} \cdot \mathbf{n} dS + \int_S \bar{\boldsymbol{\tau}} \cdot \mathbf{q} \cdot \mathbf{n} dS + \int_V \rho \mathbf{f} \cdot \mathbf{n} dV - \int_S \mathbf{q}_T \cdot \mathbf{n} dS \quad (1.17)$$

with \mathbf{q}_T the heat flux transmitted due to convection.
The conservative differential form is

$$\frac{\partial(\rho E)}{\partial t} + \nabla \cdot (\rho E \mathbf{q}) = -\nabla \cdot (p \mathbf{q}) + \nabla \cdot (\bar{\boldsymbol{\tau}} \cdot \mathbf{q}) + \rho \mathbf{f} \cdot \mathbf{q} - \nabla \cdot \mathbf{q}_T \quad (1.18)$$

while the non-conservative form is

$$\rho \frac{DE}{Dt} = -\nabla \cdot (p \mathbf{q}) + \nabla \cdot (\bar{\boldsymbol{\tau}} \cdot \mathbf{q}) + \rho \mathbf{f} \cdot \mathbf{q} - \nabla \cdot \mathbf{q}_T. \quad (1.19)$$

Working with open systems, it may be convenient to use the *enthalpy* instead of E .

$$h = e + \frac{p}{\rho} \quad (1.20)$$

Equation (1.15) is the definition of enthalpy while

$$H = \frac{q^2}{2} + e + \frac{p}{\rho} = \frac{q^2}{2} + h \quad (1.21)$$

is called *total enthalpy*. Once this quantities are introduced, the energy equation can be rearranged to obtain

$$\frac{DH}{Dt} = \frac{1}{\rho} \frac{\partial p}{\partial t} + \nabla \cdot \left(\frac{\bar{\boldsymbol{\tau}} \cdot \mathbf{q}}{\rho} \right) - \nabla \cdot \mathbf{q}_T + \mathbf{f} \cdot \mathbf{q} + Q_S \quad (1.22)$$

and the *Crocco theorem*

$$T \nabla s = \frac{\partial \mathbf{q}}{\partial t} + \nabla H - \mathbf{q} \times \boldsymbol{\omega} - \frac{\nabla \cdot \bar{\boldsymbol{\tau}}}{\rho} - \mathbf{f} \quad (1.23)$$

with

$$\boldsymbol{\omega} = \nabla \times \mathbf{q} \quad (1.24)$$

which is called *vorticity vector*. *Crocco theorem* shows how the *entropy* of a certain system changes due to multiple factors.

1.1.4 Navier-Stokes closure

$$\begin{cases} \frac{\partial \rho}{\partial t} + \nabla \cdot (\rho \mathbf{q}) = 0 \\ \rho \frac{D\mathbf{q}}{Dt} = -\nabla p + \nabla \cdot \bar{\boldsymbol{\tau}} + \rho \mathbf{f} \\ \rho \frac{DE}{Dt} = -\nabla \cdot (p \mathbf{q}) + \nabla \cdot (\bar{\boldsymbol{\tau}} \cdot \mathbf{q}) + \rho \mathbf{f} \cdot \mathbf{q} - \nabla \cdot \mathbf{q}_T. \end{cases} \quad (1.25)$$

The set of equations (1.22) has more variables than equations which implies that to be able to find one unique solution, other equations need to be included. This

problem is known as *closure*. Concerning the *shear stress tensor* it has been already introduced the *Newton Law* for Newtonian fluids. The second equation added is the *Fourier Law* for heat flux

$$\mathbf{q}_T = -k\nabla T \quad (1.26)$$

where k is the *thermal conductivity*. The remaining equations are

$$p = \rho RT \quad (1.27)$$

$$e = c_v T \quad (1.28)$$

$$c_v = \frac{1}{\gamma - 1}R \quad c_p = \frac{\gamma}{\gamma - 1}R \quad R = \frac{R_u}{M} \quad (1.29)$$

which are the *Ideal gas equation*, the definition of *internal energy* and *specific heat*. Note that R_u is the *universal gas constant* ($R_u = 8314 \text{ J/kmolK}$) and M is the *molar mass* of the specie. For an ideal gas both c_v and c_p are constants.

Now, there are sixteen equations in sixteen unknown variables which means in theory the set of equations can be solved. In reality, the analytic solution of the *Navier-Stokes equations* is unknown and it is one of the greatest modern mathematical problems. Analytic solutions exist only under specific hypotheses e.g. 1D-flow. For this reason, approximations and numerical methods are used.

1.2 Equations for reacting flows

Usually for most fluid-dynamic problems, the Navier-Stokes equations written in the previous section are every thing one needs (given the boundary conditions of course), this is not true for problems involving reacting flows in which chemistry plays a huge role. To solve these particular flows, some equations need to be added and some needs to be modified to include the reacting behavior.

1.2.1 State Equation

The state equation (already introduced in the Navier-Stokes closure problem) may be depicted as the link between chemistry and the equation of motions for it includes into the equations species and chemistry. For one to see that, equation (1.24) needs to be rewritten in a way that shows explicitly the number of moles:

$$pV = nMR_u T \quad (1.30)$$

where n is the number of moles, $R_u (= 8.314 \text{ JK}^{-1}\text{mol}^{-1})$ is the *universal gas constant*, M is the molecular weight, and V is the volume. Equation (1.27) is the most famous form of the state equation and it is usually used while working with chemical reactions (including all type of combustions). The number of moles for each chemical specie involved in such reactions is not constant, in fact normally it is a function of temperature and volume $n_i^* = n_i^*(V, T)$. The \star means that value corresponds to the thermodynamic equilibrium while subscript i stands for the i -th specie. The pressure p for a gas mixture can be calculated with *Dalton's law* under the hypotheses of equilibrium and perfect gases:

$$p = \sum_{i=1}^N p_i = \frac{1}{V} \sum_{i=1}^N n_i^* R_u T \quad (1.31)$$

For weakly compressible flows which typically include reacting gases, the pressure may be considered constant, thus

$$\rho = \frac{p_0 M}{R_u T} \quad (1.32)$$

with p_0 the ambient pressure.

1.2.2 Thermal radiation

In eq. (1.17), the only form of heat transfer considered was convection. In general, there are three way for heat to be transferred: *conduction*, *convection*, and *thermal radiation*. Conduction is not involved in this kind of problems since it is heat transfer between solid objects. On the other hand, heat transferred through radiation means becomes relevant with temperature above 600 K , easily reached during a combustion reaction. A particular spectrum of electromagnetic waves is the cause of this kind of heat exchange (only those waves which have their wave length between $0.1 \mu\text{m}$ and $100 \mu\text{m}$), this range spaces from ultraviolet radiation to infrared and includes the visible spectrum. Not all the wavelengths emit the same amount of thermal radiation, for instance infrared emissions are much more thermally conductive compared to ones of the ultraviolet spectrum. *Stefan-Boltzmann's law* describes the thermal flux due to thermal radiation:

$$q_b(T) = \sigma T^4 \quad (1.33)$$

where $\sigma (= 1.38^{-23} \text{ m}^2\text{kg s}^{-2}\text{K}^{-1})$ is the Boltzmann constant. Equation (1.33) refers to the *black body radiation*, in other words, it is written for an ideal body which emits the totality of radiations. If a real body (or *grey body*) is wanted to be taken into account, one needs to introduce the concept of *absorptivity*, *emissivity*, *transmittivity*, and *reflectivity*, then eq. (1.33) becomes

$$q(T) = \epsilon \sigma T^4. \quad (1.34)$$

The emissivity can be calculated with *Kirchhoff's law* and it is usually a function of the body geometry

$$\epsilon = \frac{q}{q_b} \quad (1.35)$$

where q_b is the heat emitted from a block body. When a thermal radiation wave hits a generic body, either a solid or a fluid, it can be absorbed, transmitted, and reflected as shown in figure (1.2)

The fraction of radiation absorbed by the body is the definition of absorptivity α , the fraction transmitted defines the transmittivity T and that part reflected is the reflectivity ρ . These fractions are linked through a simple relationship:

$$\rho + \alpha + T = 1 \quad (1.36)$$

The values of these quantities depend on the surface material, roughness, imperfections, and other characteristics.

When it comes to thermal radiation emitted by gases, things may get more complicated, in fact every equation written so far works for surfaces, but gases emit from volumes, hence, it is necessary to adapt volumes emissions into surfaces emissions. In addition, not all gases emits/absorbs at the same wavelength, for example, N_2 , O_2 , and other gases of non-planar symmetrical molecules are not affected by low-temperature radiations. Moreover, there are some gases (like CO_2 and H_2O) that emit a lot and other which do not.

One way to adapt the equations from a volume to a surface is introducing an equivalent length:

$$L_{eq} = \frac{4V}{S} \quad (1.37)$$

V is the gas volume while S is the surface interested in the heat exchange. Table exist where values of equivalent length for different cases can be found.

One last thing needs to be done to complete the radiation adapting for gases: considering the emission from the molecules inside the volume. Each molecule is treated as an energy source and their number can be associated to the partial pressure p_i . In conclusion, the heat flux emitted by a gas is

$$q_i = f(p_i, L_{eq}, T, \lambda) \quad (1.38)$$

If a volume of fluid is emitting/absorbing radiation, it is called *participating medium*.

1.2.3 Chemical reactions

A chemical reaction is when two or more substances called reactants combine to form two or more products.



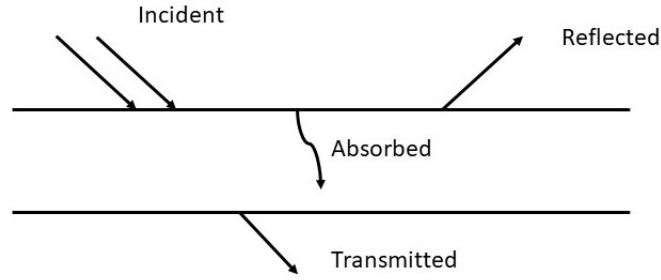


Figure 1.2: Thermal radiation hitting a body.

In the general reaction written above, N_i is the number of moles for each element that participate to the reaction. When all moles of reactants have become products, the reaction is completed, this theoretical case is also called *stoichiometric reaction*. However, usually, the number of moles of reactants is not the same of a stoichiometric case, thus not all reactants will eventually react to become product but there will be some leftover reactant.

When dealing with reactions, it is important to introduce the concept of *chemical equilibrium*. Reactions do not happen instantly, it takes some time for the reactants to react and become product. That time depends on numerous parameters (temperature, pressure, type of reaction, ...). Typically, reactions do not have a unique direction but they work both ways which means that every specie is either reactant or product.



For chemical equilibrium problems, an *equilibrium constant* can be defined as

$$K \equiv \frac{p_C^{\nu_C} p_D^{\nu_D}}{p_A^{\nu_A} p_B^{\nu_B}} \quad (1.41)$$

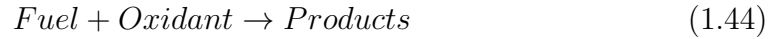
where p_i is the partial pressure of the i -th specie and ν_i is the stoichiometric coefficient. For perfect gases $K = K(T)$. The equilibrium constant can be defined also using the concentrations of the specie which take part in the reaction:

$$K = \frac{[\text{C}]^{\nu_C} [\text{D}]^{\nu_D}}{[\text{A}]^{\nu_A} [\text{B}]^{\nu_B}} \quad (1.42)$$

In reacting flows, to help determine whether the system is in chemical equilibrium, one needs to compare the reaction time and the characteristic time of the fluid-dynamic field. As it is usually done in fluid-dynamic problems, a dimensionless number is introduced: the *Damköhler number*.

$$D\ddot{a} = \frac{\tau_f}{\tau_{ch}} \quad (1.43)$$

τ_f is the fluid-dynamic characteristic time while τ_{ch} is the chemical reaction characteristic time. If $D\ddot{a} \rightarrow \infty$, the system can be considered in equilibrium since the "chemical time" is much shorter than the fluid-dynamic one ($\tau_{ch} \gg \tau_f$). On the other hand, if $D\ddot{a} \rightarrow 0$, the system is said to be "frozen" which means that even though temperature, pressure have changed, the reaction does not start and the chemical composition of the fluid remains unchanged. Things are more complicated when $D\ddot{a} \approx 1$, this means that the reaction does not have enough time to reach the equilibrium then equations become complex. To study the non-equilibrium case, it is important to understand that all chemical reactions have a certain rate meaning they develop with a defined speed. This *reaction rate* can be affected by several causes: pressure, temperature, concentrations of reactants, if a catalyst or an inhibitor is being used, thermal radiation. Just for illustrative purposes, the following generic combustion reaction is taken as example



then the reaction rate for the fuel is

$$R_{fu} = k[Fu][Ox] \quad (1.45)$$

k is the *reaction rate constant*, it "hides" the temperature dependence. The most used equation to define k is *Arrhenius's*

$$k = A_0 \cdot \underbrace{e^{-\frac{E_a}{R_u T}}}_{\text{Boltzmannfactor}}. \quad (1.46)$$

$A_0 \neq const$ but it includes all the molecular collision effects and the collision frequency:

$$A_0 = AT^n \quad (1.47)$$

E_a in the Arrhenius equation is the energy required for the reaction to activate and it is called *activation energy*. If a catalyst is involved in the reaction, the activation energy is lower than it would be without it. E_a has different trend depending on whether a reaction is exothermic, meaning that it produces heat, or endothermic which means it requires heat. It is important to know that it is not a function of the temperature and the same can be said for the parameters inside the pre-exponential factor in the Arrhenius equation

$$A, n, E_a \neq f(T, C) \quad (1.48)$$

where C is the concentration of the species that participate to the reaction. When the chemical reaction is a combustion, the reaction rate may be described

with different equations.

In reacting flows, a problem may occur regarding the system enthalpy and the one of the reaction species which has to be calculated starting from the same reference state. It is known that the mixture enthalpy is

$$H = \sum_{i=1}^n H_i = \sum_{i=1}^n m_i h_i. \quad (1.49)$$

with

$$\bar{h}_i = \bar{h}_f^\circ + \underbrace{\bar{h} - \bar{h}^\circ}_{\text{enthalpy change}} = \bar{h}_f^\circ + \int_{T_d}^T \bar{c}_p dT'. \quad (1.50)$$

\bar{h}_f° is called *enthalpy of formation* or *heat of formation*, it is the enthalpy required for producing one mole of compound in the most stable reference state with reference conditions of pressure and temperature. Enthalpy of formation values for different reactants and products can be easily found in JANNAF tables. The subtraction renamed *enthalpy change* is due to the change in temperature from the reference state (T_d).

Usually, a reaction is followed by a change in temperature where typically the final temperature is higher than the initial one. This leads to the definition of *heat of reaction* defined as the heat required to bring back the system to its original temperature which would be that of the reactants.

$$\Delta H = H_P - H_R = \sum_{i=1}^{n_P} N_i h_{fi}^\circ + \sum_{j=1}^{n_R} N_j h_{fj}^\circ \quad (1.51)$$

In combustion reactions one more notion may be helpful and it is that of the *adiabatic flame temperature*: it is the temperature which the products have under the hypotheses of adiabatic flow and it represents the maximum temperature that a reaction ideally can reach. It can be easily calculated with an energy balance of products and reactants.

1.2.4 Conservation of mass fraction

The number of moles throughout a chemical reaction it is not necessarily conserved, that is why the mass fraction is introduced.

$$Y_i \equiv \frac{m_i}{\sum_{i=1}^N m_i} \quad (1.52)$$

$$m_i = n_i M_i \quad (1.53)$$

$$\sum_{i=1}^N Y_i = 1 \quad (1.54)$$

where n_i is the number of moles for the i -th specie and M_i is its molecular weight. Mass fraction are more suited for these problems because it is always perfectly conserved in a combustion reaction.

The structure of the conservation equation it is totally analogue with the other three seen previously: the change in time of the conserved quantity plus its flux is equal to all possible sources.

$$\frac{\partial(\rho Y_i)}{\partial t} + \mathbf{q} \cdot \nabla(\rho Y_i) = \omega_i. \quad (1.55)$$

ω_i is the *production term* and it varies according to the chemical model used and it is the most complex part of the equation. Eq. (1.55) is written for $N - 1$ specie while for the N -th mass fraction

$$Y_N = 1 - \sum_{i=1}^N Y_i \quad (1.56)$$

One of the many ways to write the production term is using the *generalized finite-rate formulation*:

$$\omega_i = \frac{\partial}{\partial x_j} \left[\rho D_i \frac{\partial Y_i}{\partial x_j} \right] + R_i \quad (1.57)$$

where R_i is the reaction rate of the i -th specie which can be expressed by different laws such as the *Arrhenius form*

$$\bar{R}_{fu} = \bar{Y}_{fu} \bar{Y}_{ox} A_0 \bar{\rho}^2 e^{-\frac{E_a}{R_u T}} \quad (1.58)$$

and ρD_i is the *diffusion coefficient* expressed by

$$\rho D_i = \frac{\mu}{Sc_i} \quad (1.59)$$

Sc_i is called *Schmidt number*, it is a dimensionless parameter which compares two types of diffusion: kinematic and material. Since in reacting problems, there are numerous species involved, there are several Schmidt number. To solve this problem, usually, the value of $Sc = 0.7$ is used.

Finally, substituting equation (1.58) into (1.55) one gets

$$\frac{\partial}{\partial t}(\rho Y_i) + \frac{\partial}{\partial x_j}(\rho u_j Y_i) = \frac{\partial}{\partial x_j} \left[\rho D_i \frac{\partial Y_i}{\partial x_j} \right] + R_i \quad (1.60)$$

Once the mass fraction has been introduced, it is necessary to revisit the energy equation, in fact molecules of the mixture contribute to the diffusion of part of enthalpy:

$$h = \rho \sum_{l=1}^N h_l Y_l V_l; \quad V_l = -\frac{D_{l,inert}}{Y_l} \frac{\partial Y_l}{\partial x_j} \quad (1.61)$$

With the mass fraction, also the mixture viscosity, conductivity, and specific heat at constant pressure can be calculated:

$$C_p = \sum_{l=1}^N Y_l C_{p,l}; \quad \mu = \sum_{l=1}^N Y_l \mu_l; \quad k = \sum_{l=1}^N Y_l k_l. \quad (1.62)$$

where μ_l can be calculated with *Sutherland formula* while usually $C_{p,l} = \sum_{k=0}^K a_{k,0} T^k$ or one can use more accurate polynomials from "NASA *Thermochemical Polynomials*".

1.2.5 High temperature effects

It is well known that the temperature of any combustion properties is well above that one of standard air which is typically studied as a perfect gas. High temperatures have impact on the *degrees of freedom* of the molecules that the mixture is made out of, in fact, it is known that temperature is a way to measure molecular vibration, so an increment of temperature results in change of the distance between atoms that make molecules. The dof are one way to express the "ability" of a molecule to store energy and they depend on temperature and complexity of the molecule. The energy "carried" by each degree of freedom is:

$$e = \frac{KT}{2} \quad (1.63)$$

where $K = (1.38^{-23} \text{ m}^2 \text{ kgs}^{-2} \text{ K}^{-1})$ is the *Boltzmann constant*.

There are different types of dof but those that are of interest are: *translational*, *rotational*, and *vibrational*. All kinds of molecules have three translational dof, monatomic molecules do not have rotational and vibrational ones while a bi-atomic and tri-atomic have respectively two and three rotational dof. There is a particular case where, even though the molecule has three atoms they are aligned (e.g carbon dioxide) and that leads to only two degrees of freedom.

With the activation of more dof due to change in temperature, the composition of the mixture tends to stray further from a perfect gas. This has a direct impact on those parameter which were considered constant when a perfect gas was the model used to described the gas i.e. c_p , c_v , and the other parameters derived from these two (γ and R).

$$c_v = \frac{LR_u}{2M} \quad (1.64)$$

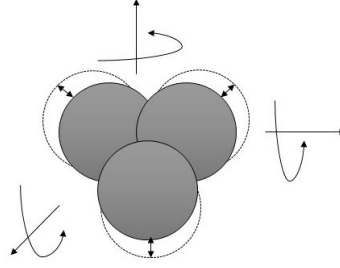


Figure 1.3: Dof for a triatomic molecule

$$c_p = \left(\frac{L + 2}{2} \right) \frac{R_u}{M}. \quad (1.65)$$

Eq. (1.65) multiplied by M can be substituted in Eq. (1.62) to find the new value for a mixture. Usually, in computational analysis as it will be shown further in this document, $c_p = f(T)$ is sum of different polynomials.

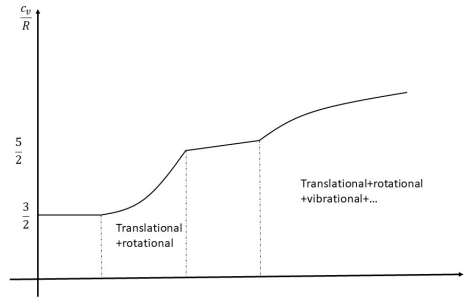


Figure 1.4: Activation of degrees of freedom (dof)

1.3 Turbulence

So far, fluid viscosity has been treated purely as some physical property as many others e.g. thermal conductivity or incompressibility. In reality it has a more central role, in fact viscosity strongly dictates the type of flow which is directly correlated to the behavior of such flow. Mainly there are two type of flows: laminar and turbulent. Laminar flows are characterized by ordered and regular streamlines

and it usually presents some form of symmetry e.g. laminar flow inside a tube. Turbulent flow on the other hand is depicted as a tridimensional "chaotic" flow which behaves randomly and can be studied using statistics. It is also characterized by the presence of circular flow structures named eddies which can be of different sizes and may dissipates energy. It is important to say that the presence of eddies does not inevitably mean turbulent flow in fact they can be found in laminar flows too.

To predict whether the flow is going to be laminar or turbulent, a dimensionless number is introduced: the *Reynolds Number*. This famous parameter allows to understand if the behavior of one flow will be characterized by its inertia or its viscosity.

$$Re = \frac{\text{Forces of inertia}}{\text{Viscous forces}} = \frac{ma}{\tau S} \sim \frac{\rho L^3 \frac{L}{t^2}}{\mu \frac{L}{tL} L^2}$$

which leads to

$$Re = \frac{\rho UL}{\mu} \tag{1.66}$$

Eq. (1.66) can be rewritten introducing the cinematic viscosity instead of the dynamic one. The cinematic viscosity is simply defined as

$$\nu = \frac{\mu}{\rho} \tag{1.67}$$

then

$$Re = \frac{UL}{\nu} \tag{1.68}$$

When viscosity prevails on the inertia of the flow, Re is low whereas when the inertia is the dominant effect on the behavior of the phenomenon, Re is high. "Low" and "high" depend on the geometry of the case e.g. flow inside a cylindrical tube, flow investing a cylinder or a airfoil, in fact, each "shape" has a different *limit Reynolds number* Re_L which represents the conventional threshold between laminar and turbulent flow. In realty, a transition zone divides the two principal regimes and once again, the range and the characteristics of such region is different from geometry to geometry.

Besides knowing whether a flow is laminar or turbulent, knowing the value of the Reynolds allows to predict and evaluate the drag coefficient of an object which strongly depends on said number.

Ascertained the turbulent nature of the flow (i.e. diffusivity and randomness are dominant), some form of analytical and statistical method needs to be used to describe it.

1.3.1 Reynolds-Averaged Navier-Stokes (RANS)

Turbulent flows still satisfy the hypotheses of continuum i.e. their motion may be described by the Navier-Stokes equations. As said in the introduction of this section, this type of flow presents chaotic fluctuations of pressure, velocity, etc... One simple approach of solving these random variations is considering each main properties as result of a mean value and the fluctuation from it:

$$\varphi = \bar{\varphi} + \varphi' \quad (1.69)$$

where

$$\bar{\varphi} = \frac{1}{\Delta t} \int_{t_0}^{t_1} \varphi(t) dt \quad (1.70)$$

Δt represents the time interval which greater than the slowest property variation (due to bigger eddies). It is important to notice that by definition

$$\overline{\varphi'} = \frac{1}{\Delta t} \int_{t_0}^{t_1} \varphi'(t) dt = 0. \quad (1.71)$$

Eq. (1.70) is used for every property appearing in the Navier-Stokes equation such as density, pressure, velocity, enthalpy and this lead to the *Reynolds-Averaged Navier-Stokes equations* often cited as *RANS*. They owe their name to the application on the NS of the *Reynolds averaging rules* which are written below:

$$\begin{aligned} \overline{\alpha} &= \bar{\alpha}; & \overline{\alpha + \beta} &= \bar{\alpha} + \bar{\beta}; & \overline{\alpha\beta} &= \bar{\alpha}\bar{\beta}; \\ \overline{\alpha\beta} &= \bar{\alpha}\bar{\beta} + \overline{\alpha'\beta'}; & \frac{\partial \bar{\alpha}}{\partial s} &= \frac{\partial \alpha}{\partial s}; & \overline{\int \alpha ds} &= \int \bar{\alpha} ds \end{aligned} \quad (1.72)$$

where α and β are the dependent variables while s is one of the independent variable i.e. x , y , z and t .

$$\frac{\partial \bar{\rho}}{\partial t} + \frac{\partial}{\partial x_j} (\bar{\rho} u_j + \overline{\rho' u_j'}) = 0 \quad j = 1,2,3 \quad (1.73)$$

$$\frac{\partial}{\partial t} (\overline{\rho u_j} + \overline{\rho' u_j'}) + \frac{\partial}{\partial x_j} (\overline{\rho u_i u_j} + \overline{\rho' u_i' u_j'} + \overline{u_i \rho' u_j'} + \overline{u_j \rho' u_i'} + \overline{\rho' u_i' u_j'}) = -\frac{\partial \bar{\sigma}_{ij}}{\partial x_j} + \overline{S_{u_j}} \quad (1.74)$$

with

$$\bar{\sigma}_{ij} = \bar{p} \delta_{ij} - \mu \left(\frac{\partial \bar{u}_i}{\partial x_j} + \frac{\partial \bar{u}_j}{\partial x_i} \right) + \frac{2}{3} \mu \frac{\partial \bar{u}_i}{\partial x_j} \delta_{ij} \quad i, j = 1,2,3 \quad (1.75)$$

$$\begin{aligned} \frac{\partial}{\partial t} (\bar{\rho} \bar{h} + \overline{\rho' h'}) + \frac{\partial}{\partial x_j} (\overline{\rho u_j \bar{h}} + \overline{\rho h' u_j'} + \overline{u_j \rho' h'} + \overline{h \rho' u_j'} + \overline{\rho' u_j' h'}) = \\ = -\frac{\partial}{\partial x_j} \left(\frac{k}{C_p} \frac{\partial \bar{h}}{\partial x_j} \right) + \overline{S_h} \quad j = 1,2,3 \end{aligned} \quad (1.76)$$

The three equations written above are respectively the *time-averaged conservation of mass, momentum, and enthalpy*. Noted that $u_{1,2,3} = u, v, w$ and $x_{1,2,3} = x, y, z$ while δ_{ij} is the already mentioned *Kronecker delta* which is equal to 1 if $i = j$ and is equal to 0 if $i \neq j$. It is equally important to observe that in most applications, the fluctuations of μ , k and C_p can be neglected.

From these equations, various turbulence models are derived. In the following subsections a brief explanations of these methods is explained not going in full details but just enough to be able to understand what is the main idea behind the models chosen for the numerical simulations. In all RANS method the mean value oscillation of the main properties is neglected, in doing so a non-negligible error is made. To solve this problem a new kind of viscosity is introduced called *turbulent viscosity*. This parameter does not have any physical meaning whatsoever but it is purely mathematical. This new viscosity includes all the energy transport and diffusion not present in the mean value. With this new parameter, the effective viscosity can be written as

$$\nu_{eff} = \nu + \nu_t \quad (1.77)$$

where ν is the physical viscosity and ν_t is the turbulent viscosity which has different formulations that depend on the model used.

1.3.2 Standard k- ϵ model

This model introduces two new parameters and two new partial differential equations that are added to the system. They are the *turbulent kinetic energy k* and the *turbulent kinetic energy dissipation rate ϵ* .

$$k = \frac{1}{2}(\overline{u'^2} + \overline{v'^2} + \overline{w'^2}) \quad [m^2 s^{-2}] \quad (1.78)$$

The formula and the name for k is self explanatory, ϵ does not have any formula describing it and it represents the velocity with which the turbulence kinetic energy is diffused. On the contrary ν_t has an explicit relation:

$$\nu_t = C_\mu \frac{k^2}{\epsilon} \quad [m^2 s^{-1}] \quad (1.79)$$

where $C - \mu = 0.09$ is the model coefficient for turbulent viscosity. As previously mentioned, there are two more equations to be written and they are k and ϵ transport equation.

$$\frac{D}{Dt}(\rho k) = \nabla \cdot (\rho D_k \nabla k) + P - \rho \epsilon \quad (1.80)$$

$$\frac{D}{Dt}(\rho\epsilon) = \nabla \cdot (\rho D_\epsilon \nabla \epsilon) + \frac{C_1 \epsilon}{k} \left(P + C_3 \frac{2}{3} k \nabla \cdot \mathbf{q} \right) - C_2 \rho \frac{\epsilon^2}{k} \quad (1.81)$$

with

- D_k = Effective diffusivity for k ;
- P = Turbulent kinetic energy production rate [$m^2 s^{-3}$];
- D_ϵ = Effective diffusivity for ϵ ;
- C_1, C_2 = Model coefficients.

For initial and boundary conditions, hypothesizing isotropic turbulence, k and ϵ are calculated with the following equations :

$$k = \frac{3}{2} (I |u_{ref}|)^2 \quad (1.82)$$

$$\epsilon = \frac{C_\mu^{0.75} k^{1.5}}{L} \quad (1.83)$$

where I is the turbulence density (usually from 0.02 to 0.05), u_{ref} is a reference flow speed typically the velocity of the flow at an inlet, $C_\mu = 0.09$ a model constant and L is a reference length like the inlet height.

1.3.3 k - ω Shear Stress Transport Model

Just like the previous model, k is the turbulent kinetic energy while ω is the turbulent specific dissipation rate [Hz]. This model too introduces two more differential equations i.e. two transport equations.

$$\frac{D}{Dt}(\rho k) = \nabla \cdot (\rho D_k \nabla k) + \rho G - \frac{2}{3} \rho k \nabla \cdot \mathbf{q} - \rho \beta^* \omega k + S_k \quad (1.84)$$

$$\frac{D}{Dt}(\rho \omega) = \nabla \cdot (\rho D_\omega \nabla \omega) + \frac{\rho \gamma G}{\nu} - \frac{2}{3} \rho \gamma \omega \nabla \cdot \mathbf{q} - \rho \beta \omega^2 - \rho (F_1 - 1) C D_{k\omega} + S_\omega \quad (1.85)$$

$$\nu_t = a_1 \frac{k}{\max(a_1 \omega b_1 F_{23}) \mathbf{S}} \quad (1.86)$$

The formulation for all the parameters like γ , β . etc. depends on the sub-model used. Like ϵ for the k - ϵ model, ω has a boundary condition relationship.

1.3.4 Reynolds Stress Transport Models

These models introduce a symmetrical tensor named *Reynolds stress tensor* $\overline{\mathbf{R}}$ and consequently one more equation.

$$\frac{D\overline{\mathbf{R}}}{Dt} = \overline{\mathbf{P}} + \overline{\mathbf{\Pi}} - \overline{\boldsymbol{\epsilon}} + \overline{\mathbf{D}} + \overline{\boldsymbol{\Omega}} \quad (1.87)$$

with

$$\overline{\mathbf{P}} = -\overline{\mathbf{R}} \cdot (\nabla \mathbf{q} + (\nabla \mathbf{q}^T)) \quad (1.88)$$

the production term. $\overline{\mathbf{\Pi}}$ is the pressure-strain term, $\overline{\boldsymbol{\epsilon}}$ is the dissipation term, $\overline{\mathbf{D}}$ is the diffusion term, and $\overline{\boldsymbol{\Omega}}$ is the rotation term. Adopting this model requires more running time for the simulation due to the presence of a transport equation for every component of $\overline{\mathbf{R}}$

1.3.5 Large Eddy Simulations (LES)

The counterpart of RANS-based models is the *Large Eddy Simulations* method. This model does not neglect fluctuations of the mean value as done in the k - ϵ for example but it provides a low-pass filter in order to solve the big scales chosen by meshing. Using a certain filter function, those small scales, which have been left out by the size of the grid, are being modeled. This way of solving the problem leads to some length and time threshold. Similarly to the RANS models, the cinematic viscosity is modified to incorporate the errors made for solving just one particular scale. In most LES simulations it is written as follows:

$$\nu_{sgs} = 0.094\Delta\sqrt{k} \quad (1.89)$$

where $\Delta = c\sqrt[3]{V_c}$ (V_c is the cell volume and c is coefficient that depends on the model adopted).

LES models are found to be more accurate than RANS ones but there is a price to pay for this accuracy, in fact their running time is much greater than that of the RANS which leads to often prefer those.

1.3.6 Smagorinsky-Lilly Model

Differently to most turbulence models, the Smagorinsky-Lilly one does not introduce a transportation equation but the turbulent kinetic energy is calculated with the solution of the quadratic equation:

$$ak^2 + bk + c = 0 \quad (1.90)$$

where

$$a = \frac{C_e}{\Delta} \quad (1.91)$$

$$b = \frac{2}{3}tr(\mathbf{D}) \quad (1.92)$$

$$c = 2C_k\Delta(dev(\mathbf{D}) : \mathbf{D}) \quad (1.93)$$

and

$$\mathbf{D} = \frac{1}{2}(\nabla\mathbf{q} + \nabla(\mathbf{q})^T) \quad (1.94)$$

Usually (as default for OpenFOAM®) $C_e = 1.048$ and $C_k = 0.094$. Concerning the cinematic viscosity

$$\nu_{sgs} = C_k\Delta\sqrt{k} \quad (1.95)$$

In conclusion, k is calculated through the velocity which makes its transportation equation useless.

1.3.7 One Equation Model

Only the k transport equation is present.

$$\frac{D}{Dt}(\rho k) = \nabla \cdot (\rho D_k \nabla k) + \rho G - \frac{2}{3}\rho k \nabla \cdot \mathbf{q} - \frac{C_e \rho k^{1.5}}{\Delta} + S_k \quad (1.96)$$

with $C_e = 1.048$ and $C_k = 0.094$.

1.4 Turbulent combustion

Combustion is nothing more than a rapid oxidation. It occurs when, in adequate quantities and properly mixed, oxidizer and fuel are "invested" by enough heat to activate the reaction. For a combustion process to be self-sustained it has to produce enough heat to trigger the reaction where oxidizer and fuel are mixed.

Depending on the physical condition and distribution of the fuel and everything that may be involved in the process, two different types of combustion and flame can be depicted. For what concerns the flame i.e. combustion products that emit electromagnetic thermal energy radiation, it can be diffusive or pre-mixed (alternatively an hybrid flame can be introduced). On the other hand, just like the flows type, combustion can be laminar or turbulent.

In a diffusion flame (e.g. candle flame), oxidizer and fuel are not initially mixed in together but they are just after the combustion process has already started. Pre-mixed flames have usually a blue colour which indicates a more efficient combustion process i.e. less un-burnt fuel.

Laminar flames, just like laminar flows are characterized by low velocities and regular and quasi-symmetrical shapes and they are not very common. In turbulent flames, the presence of eddies strongly affects the mixing process of the reactants. Also the size of these eddies is very important for the flame behavior and the thickness of its front. Concerning the large-scale turbulence, if eddies are bigger than the flame front thickness, then the laminar flame keeps its structure which may "wiggle" slightly. While small-scale turbulence only alters the effective transport coefficients thus properties transport is due to turbulent diffusivity and not due to molecular diffusivity.

For high Reynolds number, the flame structure is very irregular and complex. Turbulent flames are characterized by high combustion efficiencies thanks to the increased mixing process. With this kind of combustion, the already complex chemical processes gets even more complex due to turbulence phenomena. This entails the impossibility to consider well-detailed and articulate chemical numerical models for 2D and 3D flames, in fact, computational costs depend mainly on the number of chemical species

$$\text{computational costs} \propto N^2$$

where N is the number of chemical species present in the reactions. This leads to adopting simpler reaction mechanisms rather than tenths of reaction equations (one-step reaction, etc.).

Like the turbulent flows methods introduced in the previous section, turbulent chemistry models rely on Reynolds average rules which make the reaction rate equation time-averaged.

$$\overline{R_{fu}} = \frac{Ap^2}{R_u} \overline{T}^{n-2} \exp\left(-\frac{E_a}{R_u \overline{T}}\right) \overline{Y}_{fu} \overline{Y}_{ox} (1 + F) \quad (1.97)$$

$$\begin{aligned} F \equiv & \frac{\overline{Y'_{fu} Y'_{ox}}}{\overline{Y}_{fu} \overline{Y}_{ox}} + (P_2 + Q_2 + P_1 Q_1) \frac{\overline{T'^2}}{\overline{T}^2} (P_1 + Q_1) \left(\frac{\overline{T' Y'_{fu}}}{\overline{T Y}_{fu}} + \frac{\overline{T' Y'_{ox}}}{\overline{T Y}_{ox}} \right) \\ & + P_1 \frac{\overline{T' Y'_{fu} Y'_{ox}}}{\overline{T Y}_{fu} \overline{Y}_{ox}} + P_2 \left(\frac{\overline{T'^2 Y'_{fu}}}{\overline{T^2 Y}_{fu}} + \frac{\overline{T'^2 Y'_{ox}}}{\overline{T^2 Y}_{ox}} \right) + (P_3 + Q_3) \frac{\overline{T'^3}}{\overline{T}^3} + \dots \end{aligned} \quad (1.98)$$

with

$$P_n \equiv \sum_{k=1}^n (-1)^{n-k} \frac{(n-1)!}{(n-k)! [(n-1)!]^n} \frac{1}{n} \left(\frac{E_a}{R_u \overline{T}} \right)^n \quad (1.99)$$

$$Q_n \equiv \frac{(\alpha-2)(\alpha-1)\dots(\alpha+1+n)}{n!} \quad (1.100)$$

F represents the impact of turbulence into the reaction rate. It is assumed to be convergent. Unfortunately, this model can be applied in very few cases due to its strict conditions and that is why more applicable models will be introduced in the following subsections.

The main problem in turbulent combustion is the difference in time scale between turbulent flow phenomena and reactions which may vary (usually way shorter than turbulent mixing). This large difference leads to *fast chemistry assumption* in which it is assumed that reactions occur instantly thus not needing mean reaction rate.

One very common model largely used in commercial software today and that is included in more advanced models is the *mixed-is-burnt model* which assume that the chemistry is so rapid that equilibrium already exists at the molecular level. From these simple models, more common and advanced models are built such as *eddy dissipation concept* and *partially stirred reactor*.

1.4.1 Eddy dissipation concept (EDC)

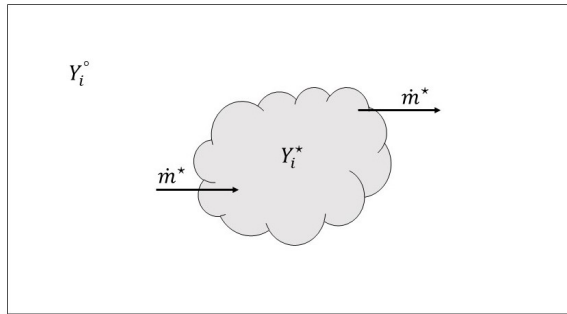


Figure 1.5: Fine structure [4]

This model divides the flow into *fine structures* in which the reactions take place. The flow fraction occupied by these structures is function of typical turbulent parameters

$$\gamma^* = 9.7 \left(\frac{\nu \epsilon}{k^2} \right)^{\frac{3}{4}} \quad (1.101)$$

while

$$\bar{Y}_i = \gamma^* Y_i^* + (1 - \gamma^*) Y_i^\circ \quad (1.102)$$

relates the mass concentration inside the fine structure and that of what is outside of it. With these new parameters the reaction rate can be written as

$$\bar{R}_i = \bar{\rho} \frac{\gamma^* \dot{m}^*}{1 - \gamma^*} (\bar{Y}_i - Y_i^*) \quad (1.103)$$

These fine structures exchange mass with the outside ambient with a certain mass transfer rate

$$\dot{m}^* = 2.45 \left(\frac{\epsilon}{\nu} \right)^{\frac{1}{2}} \quad (1.104)$$

Within the structures, different models can be applied such as fast chemistry or perfectly stirred reactor (PSR). The choice depends on the accuracy wanted and the computational cost that one is willing to pay. The first one has already been discussed and it states that combustion occurs as soon as oxidizer and fuel meet. It is cheap but not too accurate. While the PSR model describes the steady-state of a perfectly stirred reactor through these equations:

$$\frac{dp^*}{dt} = 0 \quad (1.105)$$

$$\frac{dh^*}{dt} = 0 \quad (1.106)$$

$$\frac{dY_i^*}{dt} = \omega_i - \dot{m}^*(Y_i^\circ - Y_i^*) \quad (1.107)$$

$$\omega_i = \omega_i(p, T, Y_i^*) \quad (1.108)$$

Besides these two models, the *local extinction model* may be employed. It is very simple and is based around one simple condition:

$$\tau^* < \tau_{ch} \quad \Rightarrow \quad R = 0.$$

where $\tau^* = 1/\dot{m}^*$ and τ_{ch} is the minimum residence time which allows for a sustainable combustion in a PSR and it depends on the temperature.

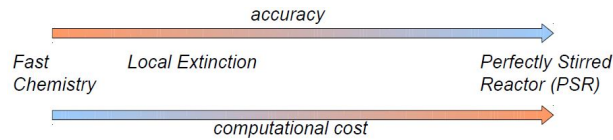


Figure 1.6: Trade between accuracy and computational cost [4]

1.4.2 Partially stirred reactor (PaSR)

The partially stirred reactor model calculates the reaction rate based on both turbulence and chemistry time scales and does so in a transient manner.

$$\bar{R}_i = k \frac{C_{i,1} - C_{i,0}}{\Delta t} \quad (1.109)$$

where k is the mixed fraction of cell that can react. This last parameter is what takes in consideration both time scale which are defined as follows:

$$\tau_m = \sqrt{\frac{k}{\epsilon} \left(\frac{\nu}{\epsilon}\right)^{\frac{1}{2}}} \rightarrow \text{turbulent mixing time} \quad (1.110)$$

$$\frac{1}{\tau_{ch}} = -\frac{1}{\rho} \frac{\partial R}{\partial Y} \quad (1.111)$$

then, by definition

$$k = \frac{\tau_{ch}}{\tau_m + \tau_{ch}} \quad (1.112)$$

In OpenFOAM®, this method is implemented slightly differently:

$$\tau_m = C_{mix} \sqrt{\frac{\mu_{eff}}{\rho \epsilon}} \quad (1.113)$$

with $C_{mix} = \frac{1}{1 + C_\mu Re_t}$ where C_μ is a model parameter.

1.5 Summary

Reacting flows are a very complex physics phenomenon which cannot be simply described by one physics branch but different aspects need to be studied. It has been showed what are the numerous equations that describes in detail all those said aspects. In order to study how reacting flows are going to behave under certain conditions, it is important to familiarize with the notion of multiple disciplines that interact with each other and are influenced by each other. It has been made clear that it is possible to describe the behavior of a fluid "simply" by writing equations for conservation of mass, momentum, and energy. It was later revealed that to solve those relationships other one needed to be taken into account thus obtaining the *Navier-Stokes Equations* which include also aspects from chemistry. Chemistry plays an extremely important role on those flows that can chemically react, so notions of chemical equilibrium and non-equilibrium where introduced and how chemical reaction are mathematically expressed and solved. Chemistry does not hold a stand alone position in the phenomenon but it is interconnected with the conservation equations which undergo some changes when chemistry is involved, thus another set of equations has been written. Radiation if taken into account has a very strong impact on the evolution of the flows since it appears on the energy equation and it can be an important source for igniting chemical reactions. Finally the concept of turbulence has been explained introducing the RANS equations and the most important and used models generated from said

equations i.e. the $k - \epsilon$ model, the $k - \omega$ model, the *RSS* model, and lastly the *LES* models. The last piece of the puzzle which is the physics inside a reacting flow phenomenon is turbulent combustion. It is explained in broad terms what are the different kinds of combustion which can occur and how they are treated mathematically and also, anticipating the next chapter, how they are handled from most commercial software.

Next chapter will be about how different methods are created in order to solve the equations written in this chapter (mostly partial differential equations) with the help of calculators.

Chapter 2

Computational Fluid-Dynamics (CFD)

2.1 Numerical methods

In the previous chapter it was explained how understanding and predicting a fluid behavior comes down to solving a set of 16 equations in 16 unknown variables. Within those 16, there are the *Navier-Stokes* equations (Eq. (1.25)) which, for exposition's sake, are re-written in their conservative form:

$$\begin{cases} \frac{\partial \rho}{\partial t} + \nabla \cdot (\rho \mathbf{q}) = 0 \\ \frac{\partial}{\partial t}(\rho \mathbf{q}) + \nabla \cdot (\rho \mathbf{q} \mathbf{q}) = -\nabla p + \nabla \cdot \bar{\boldsymbol{\tau}} + \rho \mathbf{f} \\ \frac{\partial}{\partial t}(\rho E) + \nabla \cdot (\rho E \mathbf{q}) = -\nabla \cdot (p \mathbf{q}) + \nabla \cdot (\bar{\boldsymbol{\tau}} \cdot \mathbf{q}) + \rho \mathbf{f} \cdot \mathbf{q} + \nabla \cdot (k \nabla T) \end{cases} \quad (2.1)$$

It is noticeable that these equations have a very similar structure: change in time of the quantity plus the quantity flux is equal to any possible source term. Noted that, to better handle them, it is convenient to regroup them into one simple equation:

$$\frac{\partial}{\partial t} \begin{Bmatrix} \rho \\ \rho \mathbf{q} \\ \rho E \end{Bmatrix} + \nabla \cdot \begin{Bmatrix} \rho \mathbf{q} \\ \rho \mathbf{q} \mathbf{q} + p \bar{\mathbf{I}} - \bar{\boldsymbol{\tau}} \\ (\rho E + p) \mathbf{q} - k \nabla T \end{Bmatrix} = \begin{Bmatrix} 0 \\ \rho \mathbf{f} \\ \rho \mathbf{f} \cdot \mathbf{q} \end{Bmatrix} \quad (2.2)$$

and if

$$U = \begin{Bmatrix} \rho \\ \rho \mathbf{q} \\ \rho E \end{Bmatrix}, \quad \mathbf{F} = \begin{Bmatrix} \rho \mathbf{q} \\ \rho \mathbf{q} \mathbf{q} + p \bar{\mathbf{I}} - \bar{\boldsymbol{\tau}} \\ (\rho E + p) \mathbf{q} - k \nabla T \end{Bmatrix}, \quad Q = \begin{Bmatrix} 0 \\ \rho \mathbf{f} \\ \rho \mathbf{f} \cdot \mathbf{q} \end{Bmatrix}.$$

then Eq. (2.2) can be re-written as

$$\frac{\partial U}{\partial t} + \nabla \cdot \mathbf{F} = Q. \quad (2.3)$$

Since $\mathbf{F} = f\hat{i} + g\hat{j} + h\hat{k}$, eq. (2.3) becomes

$$\frac{\partial U}{\partial t} + \frac{\partial f}{\partial x} + \frac{\partial g}{\partial y} + \frac{\partial h}{\partial z} = Q \quad (2.4)$$

with

$$f = \begin{cases} \rho u \\ \rho u^2 + p - \tau_{xx} \\ \rho uv - \tau_{yx} \\ \rho uw - \tau_{zx} \\ (\rho E + p)u - (\bar{\boldsymbol{\tau}} \cdot \mathbf{q})_x - k \frac{\partial T}{\partial x} \end{cases} \quad (2.5)$$

$$g = \begin{cases} \rho v \\ \rho uv - \tau_{yx} \\ \rho v^2 + p - \tau_{yy} \\ \rho vw - \tau_{yz} \\ (\rho E + p)v - (\bar{\boldsymbol{\tau}} \cdot \mathbf{q})_y - k \frac{\partial T}{\partial y} \end{cases} \quad (2.6)$$

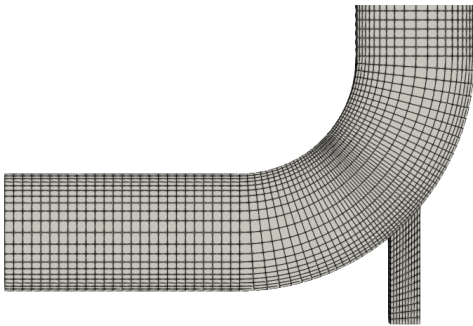
$$h = \begin{cases} \rho w \\ \rho wu - \tau_{zx} \\ \rho wv - \tau_{zy} \\ \rho w^2 + p - \tau_{zz} \\ (\rho E + p)w - (\bar{\boldsymbol{\tau}} \cdot \mathbf{q})_z - k \frac{\partial T}{\partial z} \end{cases} \quad (2.7)$$

Finding the solution to this set of equations would mean being able to calculate forces, acceleration, pressure, and other important quantities that would lead to extremely fine engineering projects. Unfortunately, eq. (2.2) is a system of partial differential equations which to this day does not have an analytic solution. This mathematical problem, together with other six problems, are called *Millennium Prize Problems* (yr. 2000). The solution to any of these problems is awarded with one million dollars by the *Clay Mathematics Institute*.

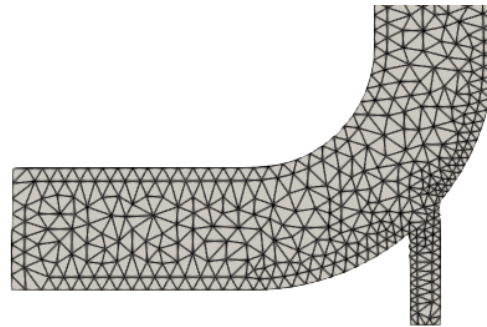
In reality, analytical solutions do exist for problems with certain hypotheses such as 1-D flow, symmetrical and adiabatic flow, and so on. Even though these special conditions can be forced to simulate and approximate some real cases, they usually fail when more complex problems need to be solved.

In order to extract some information from the equations of motion, the system

of partial differential equations is converted into a system of algebraic equations through more or less accurate approximations. This process is called *equation discretization* and it follows another important process which is *space discretization* i.e. defining the space as a set of discrete points since it is impossible to analyze an infinite number. Both processes introduce some errors. To reduce the number and magnitude of these errors, the domain should be as big as possible (a certain number of times the characteristic length of the study case) but that does not mean that bigger domains are always better, in fact bigger domains can lead to time spent to calculate quantities in useless points e.g. those belonging to an uniform part of the flow and that time has a cost. Errors magnitude also depend on the grid geometry which is very important to the point that there is a branch of CFD that is specialized only in studying grids (called *meshes*). Meshes can be *structured* i.e. made from intersection of coordinated lines, or *unstructured* meaning that is built from lines without an even pattern which does not makes it possible to number the cells in a specific order for this type of mesh. In addition, a hybrid mesh may exist i.e. one part is structured while the other is not. Where analytical methods



(a) Example of structured mesh



(b) Example of unstructured mesh

do not reach to find a solution, numerical methods are employed. Before starting with discretizing the problem, a discretization model needs to be chosen. There are three main methods:

- Finite Difference Method (FDM): historically it was the first to be used, they require a structured grid;
- Finite Volume Method (FVM): it can be employed for more complex geometry. Nowadays it is the most used method in commercial software;
- Finite Element Method (FEM): it was first employed for structural analysis than adopted by CFD but not very used. It features adaptable meshes.(Not discussed in this document)

2.1.1 Finite Difference Method

It is based on the approximation of a function through Taylor series. For exposure simplicity, at first only 1D problems are discussed.

Let the x-axis be divided into a finite number of point (N), let the distance between said point be constant and equal to Δx , if $u = f(x)$ is a generic function, then

$$\frac{du}{dx} = \lim_{\Delta x \rightarrow 0} \frac{u(x + \Delta x) - u(x)}{\Delta x}. \quad (2.8)$$

is the derivative of u with regard to x . In the discrete space, Δx would never approach zero, then the derivative can be approximated with a simple fraction:

$$\frac{du}{dx} \approx \frac{u(x + \Delta x) - u(x)}{\Delta x}. \quad (2.9)$$

In doing so, a *truncation error* is introduced. In fact, from Taylor

$$u(x + \Delta x) = u(x) + u_x(\Delta x) + \frac{u_{xx}}{2!}(\Delta x)^2 + \frac{u_{xxx}}{3!}(\Delta x)^3 + \dots \quad (2.10)$$

Eq. (2.9) can be written to highlight the error:

$$\frac{u(x + \Delta x) - u(x)}{\Delta x} = u_x + u_{xx} \frac{\Delta x}{2!} + u_{xxx} \frac{(\Delta x)^2}{3!} \quad (2.11)$$

From this equation, it is noticeable that the error dominant term is $u_{xx} \frac{\Delta x}{2!}$ which is a first order term and that leads to a first order approximation. The error could be reduced with smaller Δx even though this is not always true because instability could increase followed by an error increment.

$$u_x = \frac{u(x + \Delta x) - u(x)}{\Delta x} + o(\Delta x). \quad (2.12)$$

The first order derivative can be approximated in several ways: if $n = 1, \dots, N$, $x_n = n\Delta x$, $x_{n+1} = (n + 1)\Delta x$, and $u(x_n) = u_n$, then

$$u_x = \lim_{\Delta x \rightarrow 0} \frac{u(x + \Delta x) - u(x)}{\Delta x} \Rightarrow u_{x,n} = \frac{u_{n+1} - u_n}{\Delta x} + o(\Delta x) \quad (2.13)$$

$$u_x = \lim_{\Delta x \rightarrow 0} \frac{u(x) - u(x - \Delta x)}{\Delta x} \Rightarrow u_{x,n} = \frac{u_n - u_{n-1}}{\Delta x} + o(\Delta x) \quad (2.14)$$

This two different types of approximation are called respectively *forward* and *backward* differences. Both introduce first order errors but depending on how $u(x)$ evolves the error could be different due to the difference of slope as it is shown in

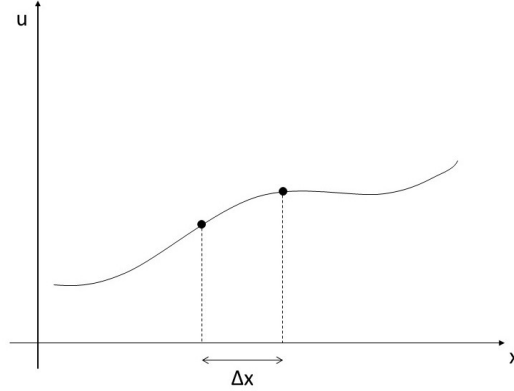


Figure 2.1: u function of x

figure (2.2).

Approximations of higher order may be created with some algebraic passages.

$$\begin{aligned}
 u_{x,n} &\approx \frac{1}{2} \left(\frac{u_{n+1} - u_n}{\Delta x} + \frac{u_n - u_{n-1}}{\Delta x} \right) = \frac{u_{n+1} - u_{n-1}}{2\Delta x} \Rightarrow \\
 &\Rightarrow u_{x,n} = \frac{u_{n+1} - u_{n-1}}{2\Delta x} + o(\Delta x^2) \quad (2.15)
 \end{aligned}$$

Eq. (2.15), called *central differences*, introduces a *second order* error as shown below:

$$\begin{cases}
 u_{n+1} = u_n + u_x \Delta x + u_{xx} \frac{(\Delta x)^2}{2!} + u_{xxx} \frac{(\Delta x)^3}{3!} + \dots \\
 u_{n-1} = u_n - u_x \Delta x + u_{xx} \frac{(\Delta x)^2}{2!} - u_{xxx} \frac{(\Delta x)^3}{3!} + \dots
 \end{cases} \Rightarrow$$

$$\Rightarrow \frac{u_{n+1} - u_{n-1}}{\Delta x} = 2u_x + 2u_{xx} \frac{(\Delta x)^2}{3!} + \dots$$

Another approximation with a second order error can be constructed starting from

$$\begin{cases}
 u_{n+1} = u_n + u_x \Delta x + u_{xx} \frac{(\Delta x)^2}{2!} + u_{xxx} \frac{(\Delta x)^3}{3!} + \dots \\
 u_{n+2} = u_n + u_x 2\Delta x + u_{xx} \frac{(2\Delta x)^2}{2!} + u_{xxx} \frac{(2\Delta x)^3}{3!} + \dots
 \end{cases}$$

multiplying the first equation by four and subtracting the second one

$$u_{x,n} = \frac{4u_{n+1} - 3u_n - u_{n+2}}{2\Delta x} + o(\Delta x^2) \quad (2.16)$$

This last approximation, although its error is of second order, it requires the knowledge of three points (or *nodes*), so it is logic to think of other more accurate

approximation involving more nodes. This gives birth to a compromise between accuracy and computational cost due to the number of points that one approximation may require. Usually commercial software use a second order approximation. The same logic is applied for higher order derivatives.

$$\begin{aligned} \frac{d^2u}{dx^2}|_n &= \frac{d}{dx} \left(\frac{du}{dx} \right)|_n \Rightarrow \\ \Rightarrow \frac{d^2u}{dx^2}|_n &= \frac{u_{n+1} - 2u_n + u_{n-1}}{\Delta x^2} + o(\Delta x^2) \end{aligned} \quad (2.17)$$

If one wants to study a multi-dimension case such as a 2-D problem, the process

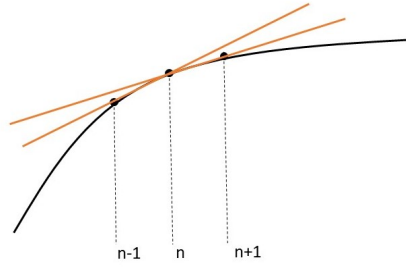


Figure 2.2: Slope difference in approximation methods

is analogous. If $\varphi = f(x, y)$ and the continuous domain is discretized into a grid with N nodes in the x direction space $\Delta x = \text{const}$ and M nodes in the y direction spaced $\Delta y = \text{const}$, $x_n = n\Delta x$, $y_m = m\Delta y$, $\varphi_{n,m} = \varphi(x_n, y_m)$, then

$$\frac{\partial \varphi}{\partial x} = \frac{\varphi_{n+1,m} - \varphi_{n-1,m}}{2\Delta x} + o(\Delta x^2) \quad (2.18)$$

$$\frac{\partial^2 \varphi}{\partial x^2} = \frac{\varphi_{n+1,m} - 2\varphi_{n,m} + \varphi_{n-1,m}}{\Delta x^2} + o(\Delta x^2) \quad (2.19)$$

$$\frac{\partial \varphi}{\partial y} = \frac{\varphi_{n,m+1} - \varphi_{n,m-1}}{2\Delta y} + o(\Delta y^2) \quad (2.20)$$

$$\frac{\partial^2 \varphi}{\partial y^2} = \frac{\varphi_{n,m+1} - 2\varphi_{n,m} + \varphi_{n,m-1}}{\Delta y^2} + o(\Delta y^2) \quad (2.21)$$

The big problem with this discretization is that the previous relationships are valid as long as $\Delta x, \Delta y = \text{const}$ and that is usually a problem in fact a rectangular grid is not suited to study basically any geometry mainly because it does not succeed in capturing the boundaries which should dictate the solution (fig. (2.3)).

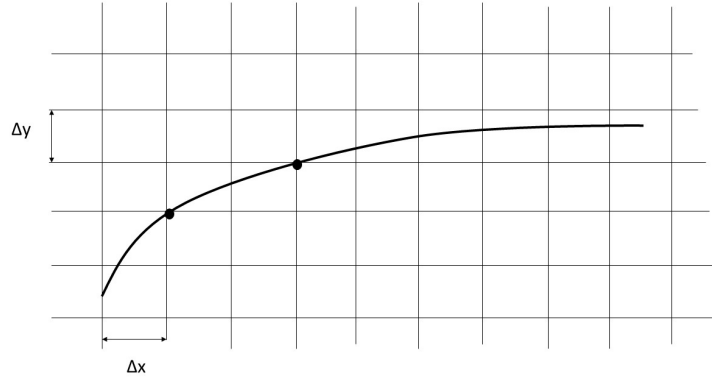


Figure 2.3: Problem capturing boundaries with constant grid

The same error can be found studying the boundary layer. Using the same Δy for the uniform region and for the boundary layer information of it would be lost. In order to capture these information, one should chose a certain small Δy which would mean having too many points in the uniform region. The solution to this and other many problems is to create adaptable grids with variable Δx and Δy and transform the physical plane (x,y) into a calculation plane (ξ, η) where the equations are solved and eventually transforming the solution for the physical plane. Of course the original set of differential equations needs to be written with the new coordinates ξ and η . Now the problem is about finding $\xi = \xi(x, y)$, $\eta = \eta(x, y)$, and the *transformation metric* i.e. $\frac{\partial \xi}{\partial x}$, $\frac{\partial \xi}{\partial y}$, $\frac{\partial \eta}{\partial x}$, and $\frac{\partial \eta}{\partial y}$. Often it is easier to find $x = x(\xi, \eta)$ and $y = y(\xi, \eta)$ which also can be used to find the transformation metric thanks the following relationships:

$$J = \frac{\partial x}{\partial \xi} \frac{\partial y}{\partial \eta} - \frac{\partial y}{\partial \xi} \frac{\partial x}{\partial \eta} \quad (2.22)$$

$$\frac{\partial \xi}{\partial x} = \frac{1}{J} \frac{\partial y}{\partial \eta} \quad (2.23)$$

$$\frac{\partial \xi}{\partial y} = -\frac{1}{J} \frac{\partial x}{\partial \eta} \quad (2.24)$$

$$\frac{\partial \eta}{\partial x} = -\frac{1}{J} \frac{\partial y}{\partial \xi} \quad (2.25)$$

$$\frac{\partial \eta}{\partial y} = \frac{1}{J} \frac{\partial x}{\partial \xi} \quad (2.26)$$

There are different ways to generate a grid so that the one on the calculation plane is rectangular and regular:

- Algebraic generation: it uses simple algebraic relationships to pass from the physical plane to the calculation plane. One example could be

$$\xi = \frac{x - x_1}{x_2 - x_1}, \quad \eta = \frac{y - b(x)}{c(x) - b(x)}$$

where the first one is basically a normalization of x-coordinate while for the second one $c(x)$ and $b(x)$ could be the walls of some case study;

- Elliptical generation: the physical domain boundaries are known and used as boundary conditions for elliptical problems:

$$\frac{\partial^2 \xi}{\partial x^2} + \frac{\partial^2 \xi}{\partial y^2} = 0 \tag{2.27}$$

$$\frac{\partial^2 \eta}{\partial x^2} + \frac{\partial^2 \eta}{\partial y^2} = 0 \tag{2.28}$$

The solution to the equations above are the coordinates of the calculation plane;

- Hyperbolic generation: it is base on carrying initial conditions through certain lines (*characteristic lines*). The intersection of these particular lines makes the grid;
- Conformal transformations: it uses analytic relationships e.g. logarithms, exponential, etc... The difficulty lies in defining the transformations for complex geometries.

In reality, there are ways to approximate derivatives according the finite difference method with non-constant intervals.

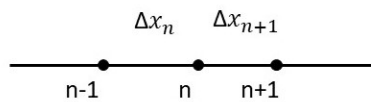


Figure 2.4: Variable intervals

$$\begin{cases} u_{n+1} = u_n + u_x \Delta x_{n+1} + u_{xx} \frac{\Delta x_{n+1}^2}{2!} + u_{xxx} \frac{\Delta x_{n+1}^3}{3!} + \dots \\ u_{n-1} = u_n - u_x \Delta x_n + u_{xx} \frac{\Delta x_n^2}{2!} - u_{xxx} \frac{\Delta x_n^3}{3!} + \dots \end{cases}$$

Combining the previous Taylor series:

$$u_{x,n} = \frac{1}{\Delta x_{n+1} + \Delta x_n} \left[(u_{n+1} - u_n) \frac{\Delta x_n}{\Delta x_{n+1}} + (u_n - u_{n-1}) \frac{\Delta x_{n+1}}{\Delta x_n} \right] + o(\Delta x_n, \Delta x_{n+1}) \quad (2.29)$$

Eq. (2.29) shows that the error magnitude depend on both Δx_n and Δx_{n+1} and this lead to the fact that if the size of the mesh elements changes abruptly, the approximation order gets worse very quickly.

Although it is possible to construct relationships such as eq. (2.29), for 2D and 3D cases they become very complex and it is not worthwhile.

2.1.2 Finite Volume Method

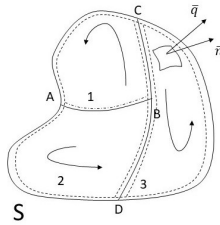


Figure 2.5: Control volume divided in three sub-volumes

This method is based on dividing the physical 3D domain into several elementary sub-volumes. These small volumes can have any shape and size, their sum needs to be the whole domain which mean there cannot be empty spaces or two volumes cannot overlap for it would generate additional source terms. So, unlike finite differences, the space is made up of volumes and not points. For each elementary volume then the conservation equations in integral form are written:

$$\frac{d}{dt} \int_V U \, dV + \int_S \mathbf{F} \cdot \mathbf{n} \, dS = \int_V Q \, dV \quad (2.30)$$

where U, F , and Q are the same quantities written for eq. (2.3). These equations are solved directly in the physical plane without the need of a calculation plane. As already said in the previous chapter, the conservative and non-conservative form of the conservation equations mathematically are completely equivalent while numerically speaking they behave differently and have different properties. Depending on which form is discretized, the numerical scheme is called *conservative* or *non-conservative*. The first scheme is more accurate for it does not introduce

additional terms when adding both side of eq. (2.30) for each sub-volume unlike the non-conservative one. Where discontinuities and/or big gradients are present, the non-conservative scheme introduces errors of non-negligible magnitude to the point where it cannot and should not be employed.

Let the volume be divided into N cells, then for the i -th cell it is possible to write

$$\frac{d}{dt} \int_{V_i} U dV + \int_{S_i} \mathbf{F} \cdot \mathbf{n} dS = \int_{V_i} Q dV \quad (2.31)$$

If the mean values are introduced

$$\mathcal{U}_i = \frac{1}{V_i} \int_{V_i} U dV \quad (2.32)$$

$$\mathcal{Q}_i = \frac{1}{V_i} \int_{V_i} Q dV \quad (2.33)$$

eq. (2.31) becomes

$$\frac{\partial}{\partial t} (\mathcal{U} V_i) + \sum_{sides} \int_{sides} \mathbf{F} \cdot \mathbf{n} dS = \mathcal{Q} V_i. \quad (2.34)$$

One last approximation can be made considering that the size of the mesh cells is a lot smaller than the domain, then

$$\frac{\partial}{\partial t} (\mathcal{U} V_i) + \sum_{sides} \mathbf{F} \cdot \mathbf{n} \Delta S = \mathcal{Q} V_i. \quad (2.35)$$

is about change in mean quantities. Nodes coordinates do not appear explicitly unlike in FDM, in fact \mathcal{U}_i can be assigned either to the cell centre, which has coordinates, or to its vertices. For a 2D case (like the one in fig. (2.6)), eq. (2.34)

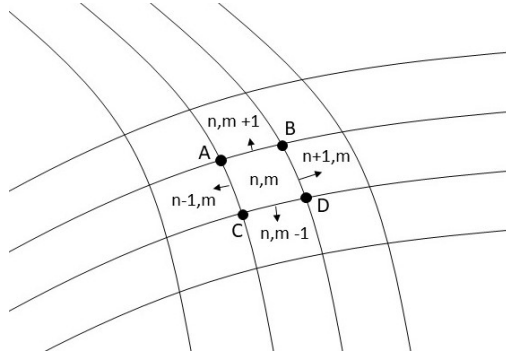


Figure 2.6: Focus on a 2D cell

is

$$\frac{\partial}{\partial t} (\mathcal{U}_{n,m} V_{n,m}) + \sum_{ABCD} \mathbf{F} \cdot \mathbf{n} \Delta S = 0 \quad (2.36)$$

if by hypotheses there are no source terms. Knowing that $\mathbf{F} \cdot \mathbf{n} = fn_x + gn_y$

$$\frac{\partial}{\partial t}(\mathcal{U}_{n,m}V_{n,m}) + \left[(fn_x + gn_y)\Delta S \right]_{AB} + \left[\dots \right]_{BC} + \left[\dots \right]_{CD} + \left[\dots \right]_{DA} = 0 \quad (2.37)$$

There can be different possibilities on how to define the flux values, in fact only the centre cell values are known which implies that values on the sides need to be constructed in some way:

$$\begin{cases} f_{AB} = \frac{1}{2}(f_{n+1,m} + f_{n,m}) \\ f_{BC} = \frac{1}{2}(f_{n,m+1} + f_{n,m}) \\ \vdots \end{cases}$$

or

$$f_{AB} = \frac{1}{2}(f_A + f_B) \quad (2.38)$$

where

$$f_A = \frac{1}{4}(f_{n,m} + f_{n+1,m} + f_{n+1,m-1} + f_{n,m+1}) \quad (2.39)$$

$$f_B = \frac{1}{4}(f_{n,m} + f_{n+1,m} + f_{n,m+1} + f_{n-1,m}) \quad (2.40)$$

and so on for the other flux values.

Usually, since the sides size is very small compared to the physical domain, they are approximated with a straight line which makes easier to calculate them. The same logic is applied for 3D cases.

2.2 Explicit and implicit numerical schemes and their properties

In order to explain what means for a numerical scheme to be explicit or implicit first a simple linear 1D partial differential equation is written:

$$\frac{\partial u}{\partial t} + a \frac{\partial u}{\partial x} = 0 \quad (2.41)$$

where $u = u(x, t)$ and $a = \text{const}$. From a numerical point of view, first thing to do is space discretization which can be done using the central difference method:

$$u_x = \frac{u_{n+1} - u_{n-1}}{2\Delta x} \quad (2.42)$$

and this leads to

$$\frac{\partial u}{\partial x}|_n = -a_n \frac{u_{n+1} - u_{n-1}}{2\Delta x}. \quad (2.43)$$

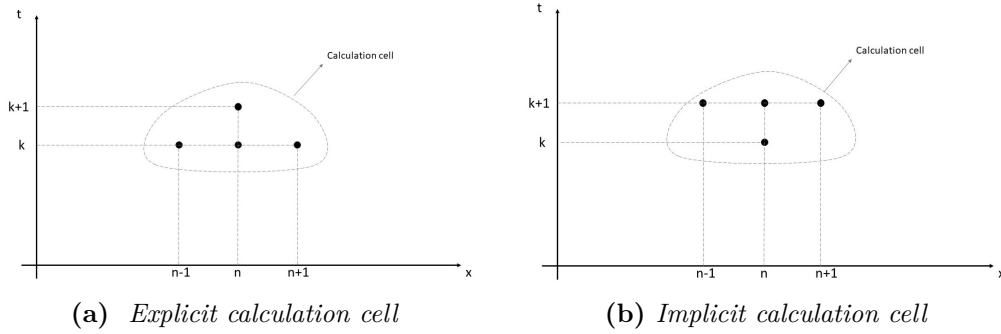
The temporal domain can also be discretized just like the physical one which means that the temporal derivative becomes

$$\frac{\partial u}{\partial t} = \frac{u(x_n, t + \Delta t) - u(x_n, t)}{\Delta t} + o(\Delta t) \quad (2.44)$$

If k is the discrete temporal step, then $u(x_n, t_k) = u_n^k$ and eq. (2.41) becomes

$$u_n^{k+1} = u_n^k - \frac{a\Delta t}{2\Delta x}(u_{n+1}^k - u_{n-1}^k) + o(\Delta t, \Delta x^2) \quad (2.45)$$

From this point, two paths can be chosen i.e. evaluate the spatial derivative in



$t = k$ or in $t = k + 1$. The first one leads to *explicit finite differences*

$$u_n^{k+1} = u_n^k - \frac{a\Delta t}{2\Delta x}(u_{n+1}^k - u_{n-1}^k) + o(\Delta t, \Delta x^2). \quad (2.46)$$

This relationship can be written for every node and it shows how the solution is obtained "*marching*" along the time. On the other hand

$$u_n^{k+1} = u_n^k - \frac{a\Delta t}{2\Delta x}(u_{n+1}^{k+1} - u_{n-1}^{k+1}) + o(\Delta t, \Delta x^2) \quad (2.47)$$

is called *implicit finite differences* and cannot be written one at a time for each node but it needs to be written simultaneously for u_{n+1}^{k+1} and u_{n-1}^{k+1} are unknown. If $\sigma = a \frac{\Delta t}{\Delta x}$,

$$-\frac{\sigma}{2}u_{n-1}^{k+1} + u_n^{k+1} + \frac{\sigma}{2}u_{n+1}^{k+1} = u_n^k \quad (2.48)$$

written for every node becomes a set of algebraic equations:

$$\begin{bmatrix} \dots & 0 & \frac{\sigma}{2} & 1 & \frac{\sigma}{2} & 0 & \dots \\ & \dots & 0 & \frac{\sigma}{2} & 1 & \frac{\sigma}{2} & 0 & \dots \\ & & \dots & 0 & \frac{\sigma}{2} & 1 & \frac{\sigma}{2} & 0 & \dots \end{bmatrix} \begin{pmatrix} \vdots \\ u_{n-1}^{k+1} \\ u_n^{k+1} \\ u_{n+1}^{k+1} \\ \vdots \end{pmatrix} = \begin{pmatrix} \vdots \\ u_{n-1}^k \\ u_n^k \\ u_{n+1}^k \\ \vdots \end{pmatrix} \quad (2.49)$$

Although the explicit scheme seems quicker, hence less expensive, it is not always convenient to employ this one due to its properties which are very different from the implicit scheme.

2.2.1 Convergence

A numerical scheme is said to converge when

$$\lim_{\Delta x, \Delta t \rightarrow 0} |\tilde{\varepsilon}_n^k| = 0 \quad (2.50)$$

with

$$\tilde{\varepsilon}_n^k = u_n^k - \tilde{u}_n^k \quad (2.51)$$

where \tilde{u}_n^k is the exact analytical solution and u_n^k is the exact value of the solution for the numerical scheme. This numerical property is very important to understand if a numerical scheme approaches the actual analytical solution, hence it can be used to simulate the motion of a fluid if the scheme solve the Navier-Stokes equations.

2.2.2 Stability

To understand this concept, first it is important to know that any real number (which may have infinity digits) needs to be represented by a machine i.e. the real number is converted into a finite sequence of bits. This process leads to a loss of information which under certain conditions can cause the numerical solution to stray further and further from the exact one. Due to computational limits, there can be different types of errors that cause instability, one of them is the *round-off error*:

$$\varepsilon_n^k = u_n^k - \bar{u}_n^k \quad (2.52)$$

where \bar{u}_n^k is a real number while u_n^k is the one represented by the machine. A scheme is said to be stable if

$$\lim_{\Delta t \rightarrow 0} |\varepsilon_n^k| < M \quad (2.53)$$

which means that if ε_n^k gets bigger and bigger each time step, then the scheme is unstable. M is the limit which needs not to be smaller than the error. It is fixed by experience and level of precision required. Very important for the stability of a numerical scheme is the *Courant number*. In order to explain its concept to a basic level, the stability of explicit numerical methods is studied through *Von Neumann stability analysis*. It is based on linear equations like many others methods even though stability studies are always very complex due to boundary conditions. Let the round-off error be the only type of error during this analysis

$$\varepsilon_n^k = u_n^k - \bar{u}_n^k \quad (2.54)$$

where \bar{u}_n^k is the exact solution of the scheme represented by eq. (2.46). Substituting eq. (2.54) into eq. (2.46) and simplifying \bar{u}_n^k , what is left is

$$\varepsilon_n^{k+1} = \varepsilon_n^k - \frac{\sigma}{2}(\varepsilon_{n+1}^k - \varepsilon_{n-1}^k) \quad (2.55)$$

which is the explicit central difference for the round-off error meaning that the error can be represented by the same identical numerical scheme as the solution. Von Neumann analysis is based on Fourier which means that the distribution of the error ε needs to be made periodic.

$$\varepsilon(x, t) = \sum_{j=-\infty}^{\infty} E_j(t) e^{i\omega_j x} \quad (2.56)$$

The equation above is the representation of the generic error function in the continuum with

$$\omega_j = \frac{2\pi}{2L} j \quad (2.57)$$

the wave number. In the discrete field, there cannot be a sum of infinite terms,

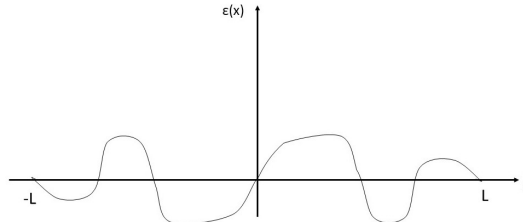


Figure 2.7: Example of generic periodic distribution in x of the round-off error

thus eq. (2.56) becomes

$$\varepsilon_n^k = \sum_{j=-N}^N E_j^k e^{i\omega_j x_n}. \quad (2.58)$$

The above equation shows that the error in a certain node and time is equal to the sum of the value each harmonic has in the n node and at k time. Since the analysis is being applied to eq. (2.41), it is possible to separate each harmonic and analyze one of them ($\omega_j = \omega$)

$$\begin{aligned} E^{k+1}e^{i\omega_n\Delta x} &= E^k e^{i\omega_n\Delta x} - \frac{\sigma}{2} \left[E^k e^{i\omega(n+1)\Delta x} - E^k e^{i\omega n\Delta x} \right] \Rightarrow \\ &\Rightarrow E^{k+1} = E^k - \frac{\sigma}{2} E^k (e^{i\omega\Delta x} - e^{-i\omega\Delta x}) \end{aligned}$$

In order for the scheme to be stable, the error must be contained i.e.

$$|G| = \left| \frac{\varepsilon^{k+1}}{\varepsilon^k} \right| < 1 \quad (2.59)$$

G is called *amplification factor* and its module needs to be lower than one for every harmonic. For this specific numerical scheme

$$G = 1 - i\sigma \sin(\omega\Delta x) \quad (2.60)$$

and its module is

$$|G| = \sqrt{1 + \sigma^2 \sin^2(\omega\Delta x)}. \quad (2.61)$$

It is possible to notice from the equation above that the centred scheme is unstable in fact $|G| < 1$, $\forall(\omega\Delta x) \in [-\pi, \pi]$, $\Delta x \neq 0$.

To complete the picture, the stability for the other numerical schemes seen is studied with the same process as before.

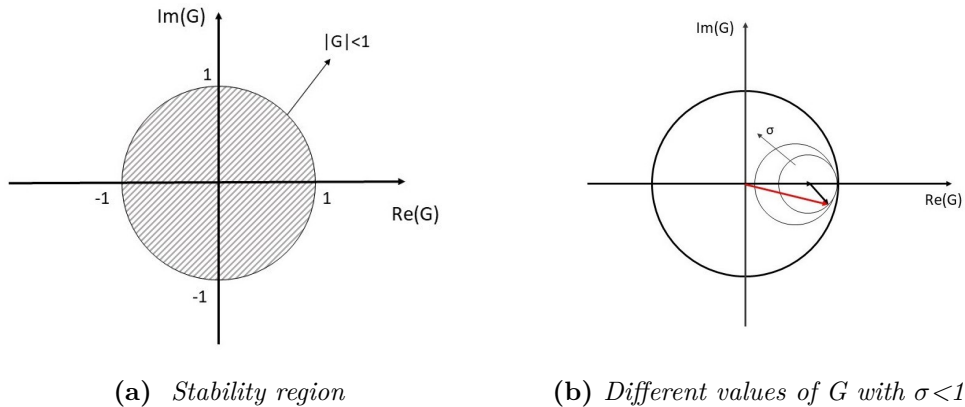
$$u_n^{k+1} = u_n^k - \sigma(u_n - u_{n-1}) \Rightarrow E^{k+1} = E^k - \sigma E^k (1 - e^{-i\omega\Delta x}) \Rightarrow G = 1 - \sigma (1 - e^{-i\omega\Delta x})$$

In this case, it is convenient to represent G through plots (fig.(2.8a) , fig.(2.8b)) Depending on the value of σ there are three different scenarios:

- $\sigma = 1$: in this case $|G| = 1$ for all values of j , in fact G describes the unit circle;
- $\sigma < 1$: G lies on a circle tangent to the one for $G = 1$ with the centre equals to $1 - \sigma$ and radius σ . G is the sum of the two vector that represent the centre and the "phase" $\omega\Delta x$, this case is stable;
- $\sigma > 1$: G lies still on a circle tangent to the one for $G = 1$ but it is always on the outside which makes this scenario unstable.

Unlike the previous scheme, the forward difference one is unstable for all σ in fact

$$G = 1 - \sigma(e^{i\omega\Delta x} - 1) = 1 + \sigma - \sigma e^{i\omega\Delta x}$$



which shows that G is always outside the unit circle which stands for stability limit. It is important to note that these stability conditions are valid for the equation (2.41) with $a > 0$. What comes out of all these examples is that the parameter $\sigma = a \frac{\Delta t}{\Delta x}$ is crucial for the stability, so important that has its own name: *Courant number*. Chosen the value for this parameter, according to stability and other numerical properties, it constrains Δt , in fact, Δx is usually fixed for it depends on how the problem geometry is meshed. This means that the temporal domain discretization cannot be arbitrary i.e. for the seen explicit schemes, in order to study a certain time arch, if Δx is relatively small, a lot of time steps are needed to describe it.

The cause of numerical instability for the seen cases can be attributed to the direction a certain information is taken from, in fact for eq. (2.41), information are "carried" along certain lines (*characteristics line*). If the numerical scheme takes information from a node which has not yet received the physical information from one of those lines, then the scheme is unstable. In figure (2.8), the black line is the analytical characteristic line from where the node $(n+1, k+1)$ takes information and it can be seen that the node $(n-1, k)$ has already received that information meaning that the numerical scheme takes information from nodes that carry the right "message". The red line shows that if Δt is too big, the numerical solution takes data from a node which carries the wrong information causing instability. Those scheme which follow the direction of the information are called *upwind* while the central schemes do not worry where they get data from.

For systems of equations the logic is the same even though when it comes to non-linear equations such as those of interest for fluid-dynamic problems, things are more complicated and the Courant number may have different definitions from the one used so far e.g. it could include the sound velocity of the i -th cell. Nevertheless, Courant number needs almost always to be smaller than one.

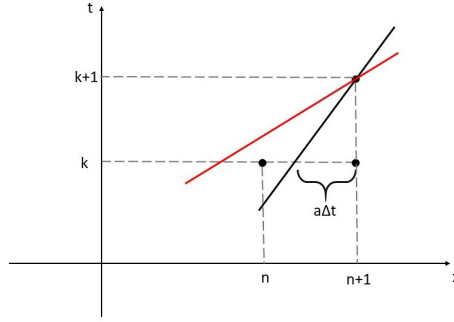


Figure 2.8: Different characteristic lines

2.2.3 Lower limit for Courant number

The nature of a lower limit for Courant number comes from another numerical property: *consistency*. A numerical scheme is said to be consistent if for $\Delta x, \Delta t \rightarrow 0$, it tends to the starting equation. To study one scheme consistency, Taylor is employed. As example, the consistency of a new numerical scheme is studied.

$$u_n^{k+1} = \frac{u_{n+1}^k + u_{n-1}^k}{2} - \frac{a\Delta t}{2\Delta x}(u_{n+1}^k - u_{n-1}^k) \quad (2.62)$$

This scheme is called *Lax-Friederichs* and it can be demonstrated that it is stable when $\sigma \leq 1$. To study its consistency, Taylor series for the three quantities appearing in eq. (2.62) are written and then are substituted into said equation.

$$\begin{aligned} u_n^{k+1} &= u_n^k + u_t \Delta t + u_{tt} \frac{\Delta t^2}{2!} + u_{ttt} \frac{\Delta t^3}{3!} + \dots \\ u_{n+1}^k &= u_n^k + u_x \Delta x + u_{xx} \frac{\Delta x^2}{2!} + u_{xxx} \frac{\Delta x^3}{3!} + \dots \\ u_{n-1}^k &= u_n^k - u_x \Delta x + u_{xx} \frac{\Delta x^2}{2!} - u_{xxx} \frac{\Delta x^3}{3!} + \dots \end{aligned}$$

After some algebraic steps, lax-friederichs becomes

$$u_t + au_x = -u_{tt} \frac{\Delta t}{2} + u_{xx} \frac{\Delta x^2}{\Delta t 2!} + o(\Delta t^2, \Delta x^2)$$

and it can be easily observed that, if $\Delta t, \Delta x \rightarrow 0$, than the scheme tends to $u_t + au_x = 0$ which is the starting equation and that means that lax-friederichs is

consistent but the numerical solution is described by another equation:

$$\begin{aligned}
 u_t + au_x &= -\Delta t u_{tt} = (au_x)_t \Delta t = \Delta t (au_t)_x = -\Delta t a^2 u_{xx} \Rightarrow \\
 \Rightarrow u_t + au_x &= \frac{u_x x \Delta x^2}{2! \Delta t} \left(1 - \frac{\Delta t^2 a^2}{\Delta x^2} \right) \Rightarrow \\
 \Rightarrow u_t + au_x &= \underbrace{(1 - \sigma^2) \frac{\Delta x^2}{2!} u_{xx}}_{=0 \text{ for } \sigma=1} \tag{2.63}
 \end{aligned}$$

Seen the purely mathematical analogy with shear stresses $\bar{\tau}$, $(1 - \sigma^2) \frac{\Delta x^2}{2!} u_{xx}$ is called *numerical viscosity*. It is important to understand that it has no physical meaning whatsoever but numerically has a dampening effect which allows the scheme to be stable. If it were not for this viscosity, the solution would "grow" each time step but this oscillation gets put under control with the viscosity. The smaller σ is, the bigger this dampening effect is and that has effects on the solution which strays further from the exact one. In conclusion, Δt needs to be as big as possible to reduce any errors caused by the numerical viscosity and to stabilize the scheme. This viscosity can be introduced artificially or be already present in the used scheme which is the case of the upwind one in fact it can be "extracted" studying the consistency:

$$u_t + au_x = a \frac{\Delta x}{2} u_{xx} (1 - \sigma). \tag{2.64}$$

Those schemes which present some kind of numerical viscosity do not bother getting information from the right direction. Since each harmonic is dampened differently, the numerical solutions strays further from the real one time step by time step. Numerical schemes also introduce a phase difference which can be analyzed through the amplification factor G.

2.3 Summary

To this day, the Navier-Stokes equations do not have an analytical solution which means that numerical methods need to be applied in order to get some useful information from them. Most of these methods relay in approximations and in minimizing those errors introduced due to the approximations. This chapter has shown that there are three main discretization methods: Finite Differences, Finite Volumes, and Finite Elements. In almost the totality of commercial software the Finite Volumes Method is employed. While the finite differences is based on using Taylor series to approximate the equations written in differential form, the Finite Volumes method divides the problem physical domain into volumes in which the

integral form of the NS equations is solved approximating the integrals into simple sums since the volumes which now the volume is made up of are relatively small. After all these concepts have been introduced, a rapid display of most common way of equations discretization has been shown e.g. upwind, central differences, and lax-friederichs. Numerical methods posses various properties which need to be analyzed in order to understand if what the calculator is solving tends to the actual solution of the problem and to do that, convergence, stability hence the important Courant number have vaguely been explained.

Now that all physical and numerical concepts necessary to analyze the study case have been introduced, it is time to proceed with the process used in order to analyze the object of this thesis.

Chapter 3

Test cases description

Two type of combustors have been selected as test cases, a classic one and an advanced one, both non pre-mixed cases. For the more classic one, the PennState pre-burner¹ was chosen while for the more futuristic combustor the geometry selected was a trapped vortex combustor². These choices were made easier for a lot of data have been gathered for said geometries and that made easier to compare experimental data with numerical ones.

As for the software used for the simulations, a license-free approach was taken. Three different software were used for the three sections a CFD simulation can be divided: meshing, calculating, and showing the result. GMSH was chosen for recreating the geometry and to generate the mesh. OpenFOAM[®] was used to perform the actual CFD calculations i.e. solving the algebraic equations obtained after time and space discretization, finally, paraview as a post-process interface to show the results. Among all the different solvers for chemical reactions that openFOAM offers, the solver reactingFoam was chosen for it has the capability to solve transient problems with compressible, laminar or turbulent reactive flows. It was selected especially or its abilities to solve non pre-mixed combustion.

ReactingFoam, as well as the other openFOAM solvers, divides its work into three main directories: 0, constant, and system. In the 0 directory the boundary conditions are written into many files as the quantities to be calculated including all the turbulence ones if a turbulent approach is taken. In this directory not only the classical fluid-dynamic properties are stored but also the mass fractions of the elements taking part to the chemical reaction. With that, a particular file called *Ydeafault* is present, this file gathers in one single element all those chemical species which are not present initially in the system but are later created. In the *constant*

¹5.

²6.

directory, reactingFOAM stores all those file concerning the chemistry properties such as the reactions to be solved, the solver which should solve them. In the same directory, a file specify whether the flow will be turbulent or laminar and what method of turbulent flow one wants to use e.g. k-epsilon, k-omega, etc., also the thermophysical properties of the flow such as Sutherland approximation for viscosity and Janaf tables for polynomial approximation of C_p . Finally, in this directory, one can specify if it wants to take into account the force of gravity (or an arbitrary g-force e.g. rocket acceleration), radiation properties and one can put the *fvOptions* file used for external sources e.g. radiation properties or to limit the temperature as well as simulating a spark through a sudden outburst of enthalpy. The final main directory is the system directory. In this folder, three files need to be always present i.e. *controlDict*, *fvSchemes*, and *fvSolution*. As the name suggests, in *fvSchemes* all the numeric schemes used to discretize space and time are written. In *fvSolution*, the numerical methods applied to solve the sets of algebraic linear equations are chosen as well as the pressure-velocity linking method (SIMPLE, PISO, or PIMPLE). Here one can set the limit to number of iterations and so on. Lastly, in the *controlDict* file are the time step chosen for the simulation or the max Courant number if it is set, the write interval and more options of this kind. In the system directory, one can put many *Dictionary-type* files for many applications such as making the mesh through *blockMesh*, or create some geometry sets or even set different initial conditions in different regions and so on.

As one can understand, the advantage of having an open source software is that it can be manipulated how one may need, in this case by adding the files necessary to make openFOAM perform certain tasks.

3.1 Advanced Vortex Combustor (AVC)

This combustor is part of the *trapped vortex* family which, as the name suggests, are able to trap eddies in between cavities in order to increase the residence time of reactants increasing the mixing and, consequently, the combustion process efficiency i.e. less unburnt fuel and less NO_x thanks to controlled temperatures due to fresh air sucked in by eddies. This geometry may be applied in classic turbofan engines with improved combustion technologies or may be used in supersonic and hyper-sonic engines for the air entering the chamber may be close to supersonic velocities which means that it does not need to be decelerated too much thus the pressure loss is kept to minimum levels.

The fuel used in this simulation is plane methane (CH_4) and the oxidizer is just air (23% O_2 , 77% N_2). Ideally this geometry can be used with liquid hydrogen as fuel for high-Mach applications since it has higher heating value than most fuels. Huge heating values are absolute necessary when talking about high-Mach engines since

the air entering them at has already high values of energy and it would be difficult to increase it if it was not for using hydrogen.

3.1.1 Geometry

The geometry used for this simulation is a 2D adaptation of the one studied in [6]. The major difference between Zeng’s geometry and this one is on the fuel inlet holes. Originally the fuel is inserted in the chamber through three circular holes with diameter D that may vary from 3 to 6 mm but in this study the value of 5 for D/mm is used. To adapt it for a 2D simulation, a simple proportion relationship was applied:

$$L = \frac{A}{t} = 0.59 \text{ mm} \quad (3.1)$$

where $A = 3\pi D^2/4$ is the area of the three injection holes while $t = 100 \text{ mm}$ is the thickness of the combustion chamber. Besides that, the geometry is basically the same: a rectangular chamber 400 mm long and 100 mm high with a front blunt body (80 mm \times 60 mm) used to obtain a 36 mm long cavity together with a rear blunt body. This last body may have different geometries which affect the evolution of the flow and combustion products. The geometry chosen is on open rear blunt body with a 2 mm slot and the half open angle θ of 50 degrees, height of 42 mm and length of 20 mm (fig.(3.1)). The slot height and the half open angle

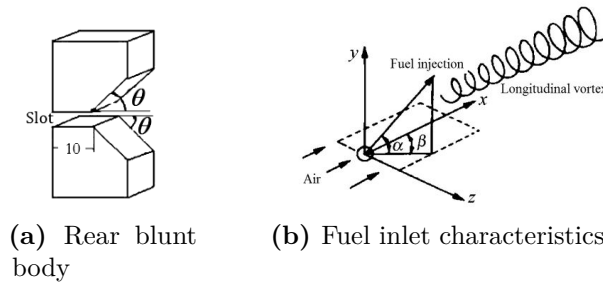


Figure 3.1: Geometric details for the fuel inlet and the second blunt body [6].

value were chosen from a selection of different values tested in Zeng’s work for they were the optimum in terms of temperature and combustion efficiency. The air intake is what remains of the chamber height minus the front blunt body height which means that its inlet is 10 mm wide.

3.1.2 Numerical setup

The Navier-Stokes equations are solved numerically using local Euler method for the time derivative i.e. known the max Courant number, for each cell the time step

calculated may be different meaning that initial solution does not have a physical meaning because each cell "sees" a different time but with later iteration the solution has physical meaning. This method is called pseudo-transient method. As for the gradient, linear scheme was employed which is a second order central difference scheme. To discretize the divergence operator, the limited linear scheme was chosen which is the same as the linear scheme previously mentioned but it employs a limiter function to avoid non-physical values. For the laplacian term also a linear scheme was used but a corrected one (for any non-orthogonal correction). The PIMPLE algorithm is used for pressure-velocity coupling which is a mix between the SIMPLE algorithm and the PISO algorithm (fig.(3.2)). All discretization and

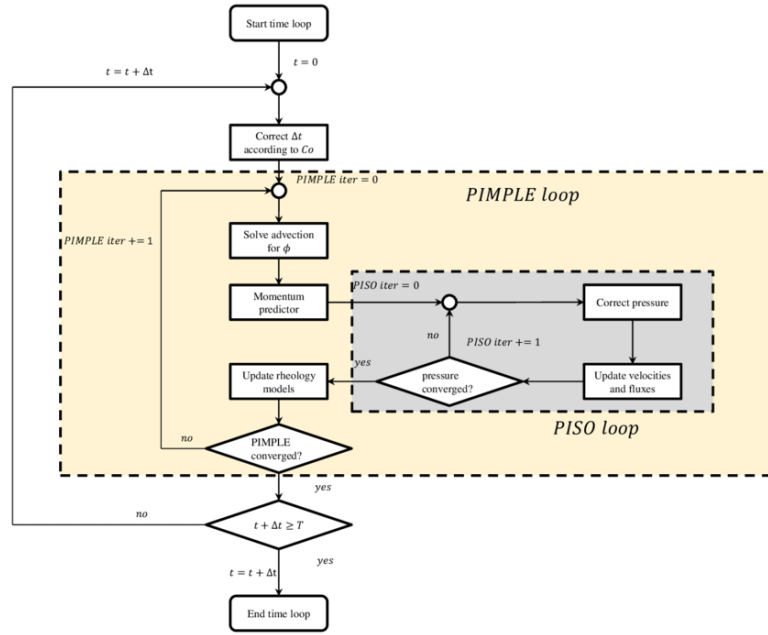


Figure 3.2: PIMPLE algorithm flow-chart [7]

matrix solving schemes can be found in appendix. Standard k-epsilon model for turbulence is used. Eddy-dissipation concept is applied for calculating reaction rate for the turbulent combustion process. In order to obtain a quick and first order solution, the reaction mechanism is made of simply one reaction i.e. methane and oxygen combustion: $\text{CH}_4 + 2\text{O}_2 \rightleftharpoons \text{CO}_2 + 2\text{H}_2\text{O}$. To calculate the viscous and thermal property of each element present in the simulation, the Sutherland and Janaf approximations are employed.

The computational mesh is structured, it is made of roughly 20000 cells (20719). To capture the boundary layer as good as possible (with limitation to first order approximation) in order to avoid any flame return from the cavity to the fuel inlet, the mesh is slightly more dense on the air inlet walls (fig.(3.4)).

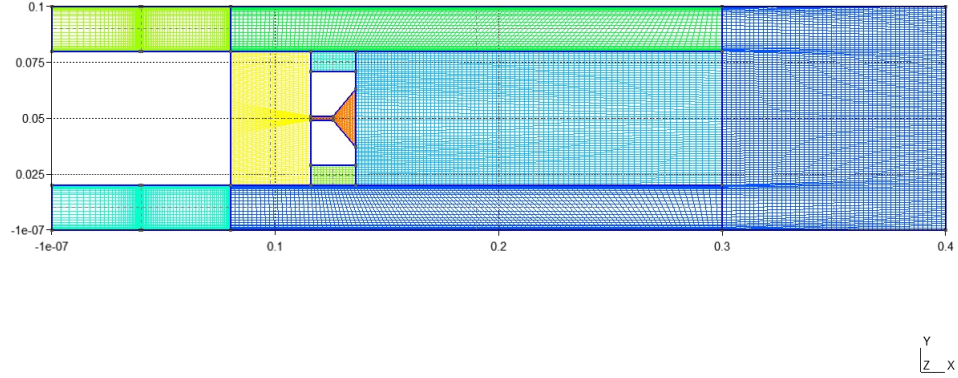


Figure 3.3: Mesh generated with GMSH for the AVC geometry

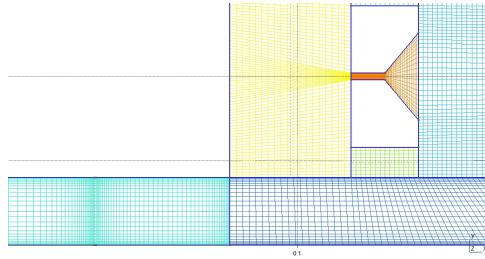


Figure 3.4: Detail of first cavity from the AVC mesh

3.1.3 Initial and boundary conditions

Four different cases have been tested in order to study its behavior with different inlet velocities to understand if it may be employed for high speed flight conditions e.g. for RAMJet engines. The four case see the air entering the combustor with increasing velocities: 25, 50, 75, and 100 m/s. For every case, the air enters the chamber with uniform temperature at 300K. Both temperature and velocity have uniform distribution and for the inlet the pressure boundary zeroGradient is employed. For the fuel injection velocity an $R = u_f/u_A = 1.5$ is adopted which means that the fuel jet entering the chamber has its velocity equals to 37.5, 75, 112.5, and 150 m/s of magnitude. The fuel is injected in the chamber with $\alpha = 60^\circ$ and $\beta = 0^\circ$, hence no longitudinal eddies are generated in order to maintain a 2D geometry. The fuel has the same temperature of the air inlet and the pressure is set to zeroGradient as well. As for the outlet patch, a static fixed pressure values of 1 atm is applied. The chamber walls including the left side of the first cavity are

isothermal ($T = 1000\text{ K}$), while for the built-in rear blunt body a zeroGradient condition is imposed. For all walls a no-slip condition is used.

In order to obtain a smooth ignition of the reacting mixture, at $t = 0$, the combustor is filled with non-moving air at $p = 101325\text{ Pa}$ and $T = 2000\text{ K}$. Equations 1.82, 1.83, and 1.79 were used to calculate k , ϵ , and ν_t at both air and fuel inlets. Wall functions were used for said quantities values. Front and back plane are set empty in order to simulate a 2D case.

3.2 Penn State pre-burner

Following the experiments done at the Pennsylvania State University’s Cryogenic Laboratory, this test case is studied purely to validate openFOAM as a reliable CFD tool.

As the title specifies, this combustor chamber is not the main one for a rocket engine but it is employed as a pre-combustor for a hybrid or liquid rocket engine which may use a staged-combustion process (open/close cycle). Gaseous hydrogen is employed as fuel while the oxidizer is gaseous hydrogen. Parts of water are present both in the oxidizer and in the fuel but in different quantities: 5.5% for the oxidizer and 59.8% for the fuel.

Due to the axial-symmetry of this case, the simulation is run as such..

3.2.1 Geometry

The pre-combustor is made of three main parts: injector, main chamber, and water-cooled nozzle. The entire combustor is cylindrical i.e. it is axial-symmetric. The injector is made of two coaxial elements: an inner cylinder for the oxidizer and an outer duct of non-constant radius for the fuel. The inner tube is slightly

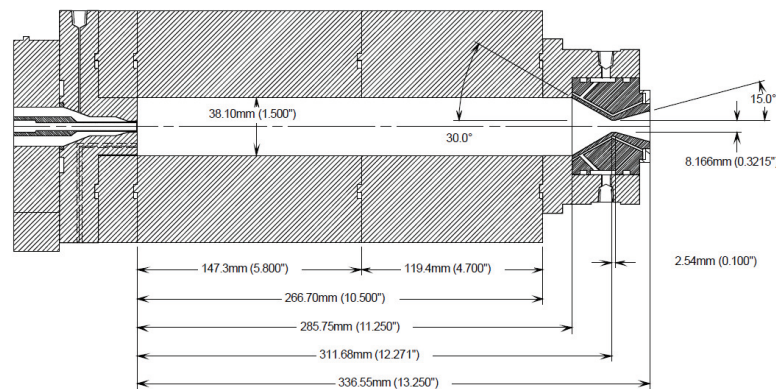


Figure 3.5: Detailed schematic of pre-combustor[8].

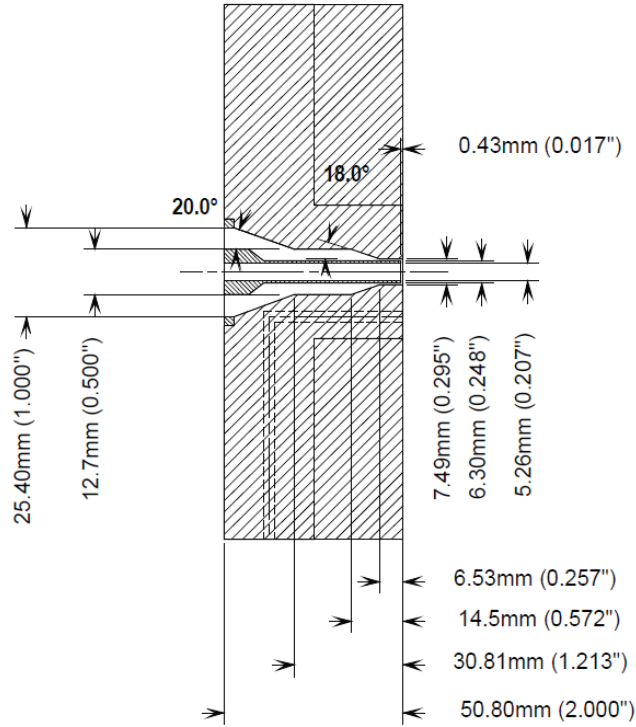


Figure 3.6: Detail of Penn State injector[8].

shorter than the outside one. All detailed measurement can be found in figure 3.6. The main chamber is a simple 38.1 mm diameter 285.75 mm long cylinder. The chamber ends with a conic convergent-divergent nozzle whose throat is made of a spline passing through three points $(15, 17, 16)$ of (x, y, z) coordinates $(4.15, 0, 311.68, 1)$, $(4.058, 312.95, 1)$, and $(4.15, 0, 314.22, 1)$.

3.2.2 Numerical setup

NS equations are solved numerically with a local Euler method for the time derivative (just like the AVC case) with maximum Courant number of 0.5, linear scheme for the gradient operator, limited linear for the divergence and linear corrected for the Laplacian term. PIMPLE algorithm is used to couple pressure and velocity. The k-omega SST (Shear Stress Transport) model for turbulence is used due to its excellent wall treatment calculations. In order to get first approximation results to refine in later works, a single step reaction model is employed to simulate combustion between oxygen and hydrogen with 4 elements and 3 species: $2\text{H}_2 + \text{O}_2 \rightleftharpoons \text{H}_2\text{O}$. The eddy-dissipation concept is applied for calculating reaction rates for the turbulent combustion [9]. Sutherland and Janaf

approximations are employed for transport and thermophysical properties. In order to run an axial-symmetric simulation, the 2D figure is rotated 0.5 degrees around the z-axis (which is the symmetric axis) clockwise and then it is extruded counter-clockwise 1 degrees around the same axis creating a small 3D figure required by openFOAM to run axial-symmetric case. The mesh is structured and made of 59128 cells. It is denser in the injector exit where both fuel and oxidizer mix with one another and reach high velocities, potentially transonic ones (fig.(3.7)).

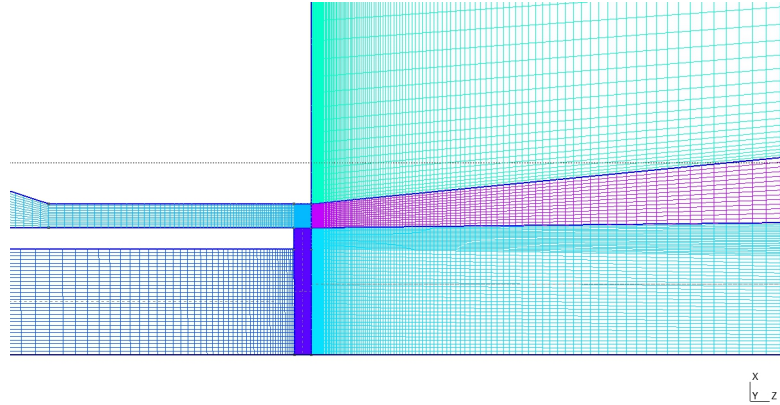


Figure 3.7: Detail of computational mesh near the injector exit

3.2.3 Initial and boundary conditions

The initial and boundary conditions for this case are chosen to replicate in the best way possible the experimentation done at Penn State [8] with some small changes made in order to reach convergence the quickest.

For both fuel and oxidizer inlet, a pressure fixed value boundary condition is chosen: $P_f = 6.5 \text{ MPa}$, $P_o = 5.85 \text{ MPa}$ while the velocities b.c are set to zeroGradient. The fuel is fed with $T = 811 \text{ K}$ while for the oxygen $T = 700 \text{ K}$. For the outlet patch, a pressure b.c. condition is chosen as well but slightly different, in fact, due to possible supersonic velocities at the divergent part of the exit nozzle, some strange things may happen with shock waves which could see the exit patch as a solid wall which may make them "bounce" back. To avoid that a waveTransmissive boundary condition is employed with $P = 3.26 \text{ MPa}$, while the temperature b.c. is set to zeroGradient. The left vertical chamber wall has fixed temperature of 755 K while for the chamber walls a *non uniform* fixed value b.c. is employed to replicate the temperature distribution measured in the Penn State experimentation. A very brief and simple MATLAB script was written to extract temperature trend and values to put in the openFOAM list (see appendix). The temperature at the nozzle

wall is also fixed for it is supposed to be a water-cooled nozzle i.e. $T = 510\text{ K}$. In order to simulate a 2D axial-symmetric flow, openFOAM requires the front and rear plane to be set as wedge patches, in addition, the axis of symmetry needs to coincide with one of the three Cartesian axis. To obtain a smooth ignition of the mixture, the chamber is filled with nitrogen at $T = 1500\text{ K}$ and $P = 3.24\text{ MPa}$ while the injector is filled for three initial quarters with their fluid at the inlet conditions of temperature and pressure while the remain quarter is filled with nitrogen with the same characteristics of the main chamber.

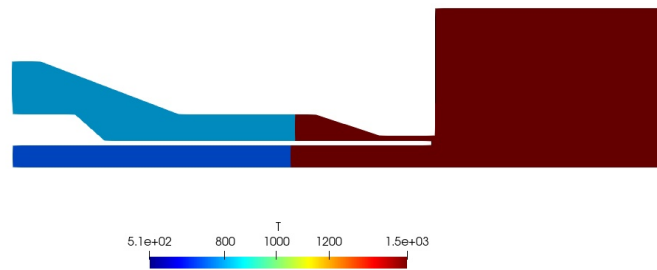


Figure 3.8: Penn State initial conditions

Chapter 4

Results

4.1 AVC

The main focus for this study is to understand if an advanced vortex combustor (or dual trapped vortex combustor) is suitable for replacing current generation engine combustors in order to satisfy *Flightpath 2050* requirements.

Using a very simple chemical mechanism, one can only focus the results on temperature profiles, CO₂ distribution and concentration, unburnt fuel (CH₄) exiting the chamber with a quick calculation on the combustion efficiency in terms of how much fuel exits the combustor with respect to how much enters it. For all four studied cases, the distribution of main physical characteristics on the exit section are plotted and compared. Finally, a detail look at the symmetrical eddies forming inside the cavity is shown as well as the *Von-Karman*-like vortices after the second blunt body.

4.1.1 Fluid-dynamic

The fluid-dynamic evolution of the flow is easily predictable and the results obtained meet the expectations for the first part while they might disagree for the second part of the flow. As one can see from fig.(4.1), the boundary layer on the inner part of the combustor increases after the fuel is fed into the ducts and separates in the wedge of the front blunt body and in doing so the flow creates two symmetrical eddies with opposite angular velocity in fact the top one rotates clockwise while the bottom one spins counterclockwise. It is also noticeable that, through the small slot, some part of the fluid can be exchanged from the second part of the flow with the two vortices.

The second part of the flow, that one after the rear blunt body also develops into eddies but they are not regular (contrary to what Zeng's et al [6]) but they remind the same pattern of *Von Karman eddies*. Fig.(4.2) shows the mechanism of

vortex creation behind the rear blunt body. Those vortices do have an effect on combustion products displacement as shown further in this chapter. This periodic phenomenon is not strong enough to destabilize the flame which is restrained in the core of the combustor.

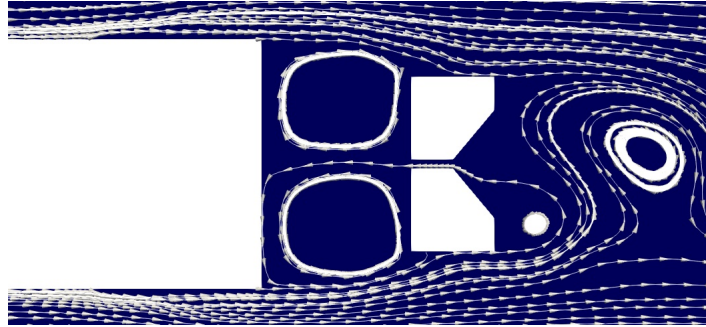


Figure 4.1: Detail of streamlines inside the cavity

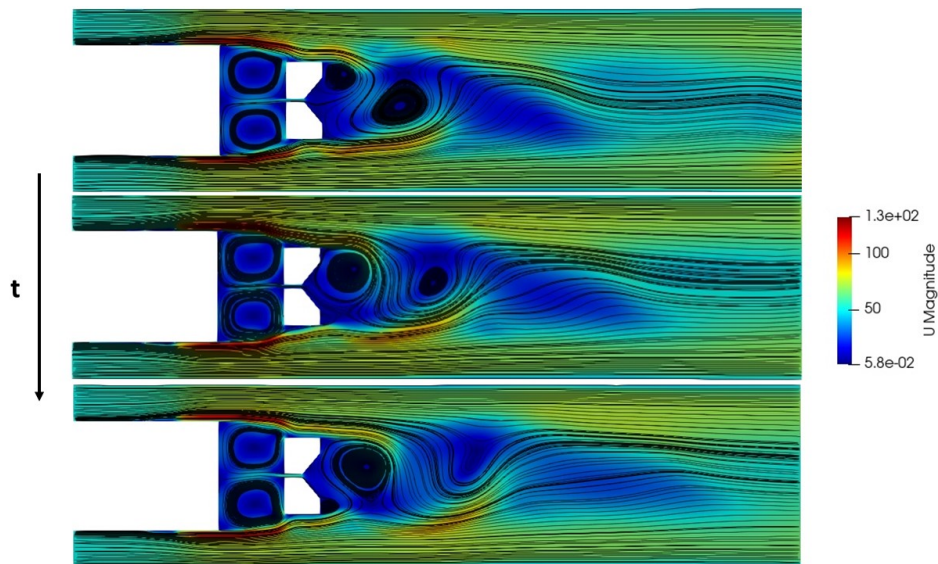


Figure 4.2: Eddies evolution through time for $U_a = 50 \text{ m/s}$

For the sake of completeness, the velocities profile at the outlet section have been plotted showing that every thing looks as it should be and one can notice that the relative minimum point at the center of the flows which corresponds more or less to the center of the hot gases is proportionally inverse to U_a . Finally, it is very noticeable the boundary layer near the chamber walls, one could eventually calculate the shear forces knowing the velocity gradient at the wall.

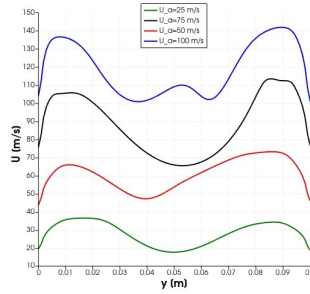


Figure 4.3: Outlet velocity profile

4.1.2 Temperature distribution

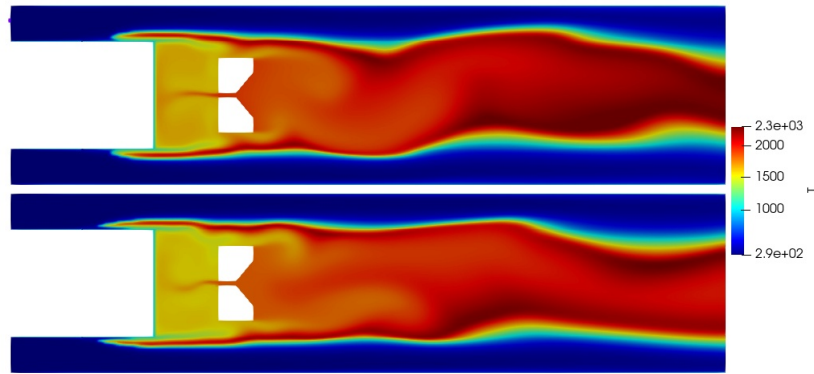


Figure 4.4: Temperature profiles for $U_a = 50 \text{ m/s}$ (top) and $U = 100 \text{ m/s}$ (bottom)

Visualizing the temperature profiles is important for it suggests where possible refinements in geometry need to be made and/or where the working condition of this "machine" needs to be.

As one can see in fig.(4.4) and fig.(4.5), for all four cases, the temperatures profiles are very similar in shape and values with the maximum value spacing from 2300 K to 2400 K . Three different areas may be noticed: the cavity between the two blunt bodies, the flame development following the built-in blunt body, and the chamber walls.

Concerning the chamber walls, it is easily noticeable that a part of the air entering the combustor (whether at 25 m/s or 100 m/s) does a great job isolating the walls from the hot core, to be reminded that the chamber walls temperature was set to fixed value of 1000 K to simulate a very poor cooling system. This results demonstrate that the AVC geometry self-constrains the heat of the combustion, hence not a complicated cooling system is required e.g. small holes on the external

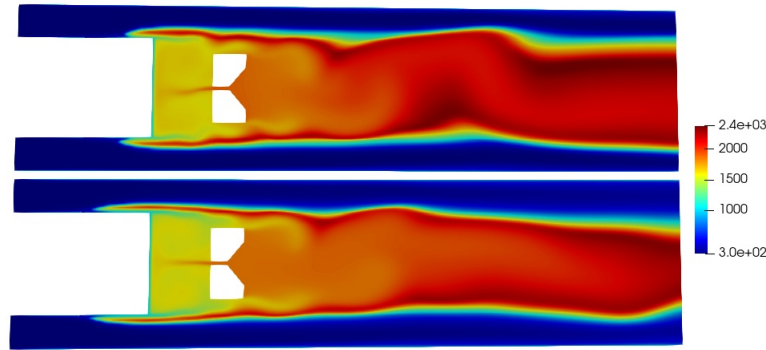


Figure 4.5: Temperature profiles for $U_a = 75 \text{ m/s}$ (top) and $U_a = 25 \text{ m/s}$ (bottom)

walls for cool air entering the chamber.

A different story needs to be told for the walls of both blunt bodies. Just like the external chamber walls, the wall of the first body are set to 1000 K and the causes that thin green line coasting the wall to the right of the vertical wall suggesting temperatures of 1400 K (seen the temperature legend at the right of the images). This kind of temperatures may require a non-negligible effort on cooling that part of the combustor. Same story for the built-in blunt body which is invested with high temperatures that may compromise its structural integrity and its purpose, hence, some sort of cooling is required.

For what concerns the cavity, an average temperature of 1700 K can be observed which is lower than the maximum temperature reached during the combustion process and development of the flame. This not so high temperatures may be the consequences of two factors one being that the combustion process is just starting and it is not fully finished and the other being that the fresh cool air sucked in by the eddies helps lowering the temperature. What may stand out from the images it the the combustion process somehow begin before the cavity, in fact an increase in temperature can be observed after the fuel inlet which is never reached and that is good since that would mean the the combustion could enter the CH_4 inlet causing a lot of damage. That hot layer is exaggerated by forcing the simulation to be 2D where in reality the mass flow would have more room making the layer thinner.

The last zone of main focus is the flame development where the maximum temperatures are reached. As previously said, the flame is contained by the fresh air. The flame temperatures after the second blunt body are still affected by the flow inside the cavity, hence they are lower than the ones at the outlet. The width to which these lower temperatures reach depends on how the second couple of eddies develop but it seems that the lower the inlet velocity of the air is, the wider this colder

zone is. Two finally observation can be made for the temperature distribution: the maximum temperatures seem to be reached where the flow takes "sudden" turns due to eddies evolution (fig.(4.2)) while in going towards symmetry axis the flame is colder; the small slot functions as a link between the hot gas of the developed flame and the colder one in the cavities and that helps the combustion to keep on going.

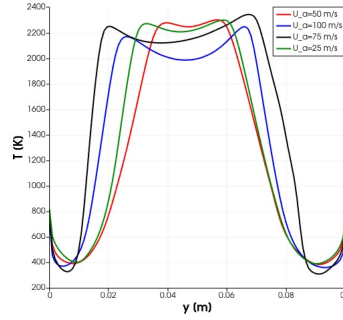


Figure 4.6: Outlet temperature profile

The plot in fig.(4.6) compares the different temperature at the outlet for the four cases that may be interest of those engineers designing the turbine blades (if present). It is clear that the higher the velocity is, the lower the maximum temperature is reached and that is probably due to the less time the mixture has to complete the combustion process. While for the minimum temperature, it is fair to said that it is not affected by the velocity. One more thing it is noticeable i.e. the width of the flame which seems to be also depending on the velocity with minimum values for $U_a = 50 \text{ m/s}$ but result may not be definite. On the contrary it is clear that the higher the velocity, the wider the flame is. One can observe two point of maximum at the extremes of the flame, those may be results of two different flows meeting i.e. hot flame and cold fresh air. Finally, a very steep gradient can be observe next to the walls due to their fixed value.

4.1.3 CO₂ distribution

The CO₂ displacement in the chamber resembles the temperature one and that is simply because those high temperatures are due to hot products of the combustion process that in this case are CO₂ and H₂O (ideally with a more complex reaction mechanism one would have more than two products). The distribution of CO₂ and H₂O are identical, hence the H₂O will not be discussed (fig.(4.7)). From the distribution of CO₂, one can clearly see where the combustion process takes place. For all four cases, the temperature and mixing condition just before the cavity are enough to activate the combustion as the images show (fig.(4.8), fig.(4.9)).

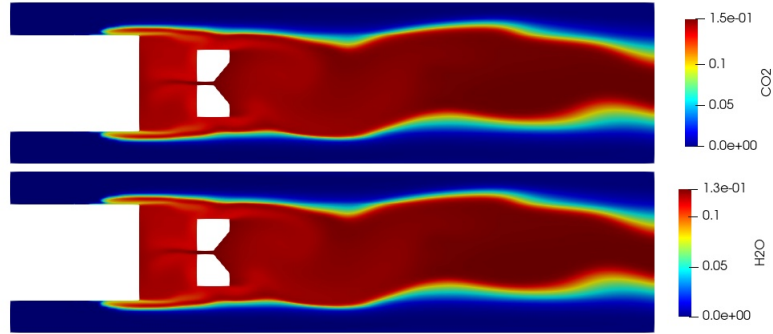


Figure 4.7: Comparison of CO_2 distribution and H_2O distribution for $U_a = 50 \text{ m/s}$

Again, the thickness of that products layer may be thinner in a 3D case because the flow has more room. It is possible to notice in the external zones of the cavity a thin, more yellow part indicating less CO_2 due to the more abundant presence of methane (as seen from fig.(4.11) and fig.(4.12)). Just like with the temperature, the blue zone near the combustor external walls highlight the containment of the flame in the core of the chamber.

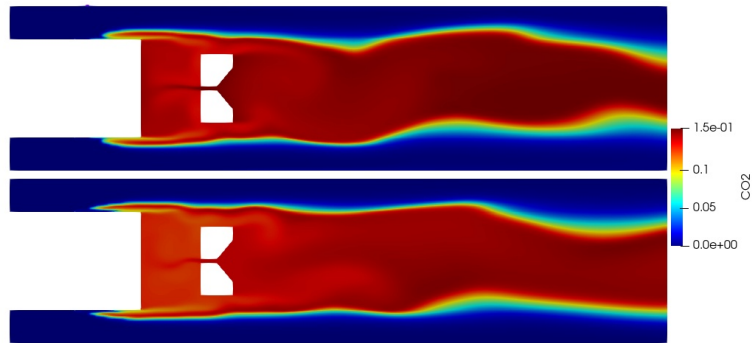


Figure 4.8: CO_2 distribution for $U_a = 50 \text{ m/s}$ (top) and $U = 100 \text{ m/s}$ (bottom)

Contrary to the temperature, concerning the CO_2 mass fraction at the outlet section, it seems that does not strongly decrease proportionally to the air inlet velocity, in fact, besides the width of the peak, the maximum value is very similar for $U_a = 25, 50, 75 \text{ m/s}$, while one can notice slight drop for $U_a = 100 \text{ m/s}$ which may be mainly due to the presence of more unburnt fuel exiting the chamber, hence less combustion product. While for the peak width it does not appear to follow some kind of trend.

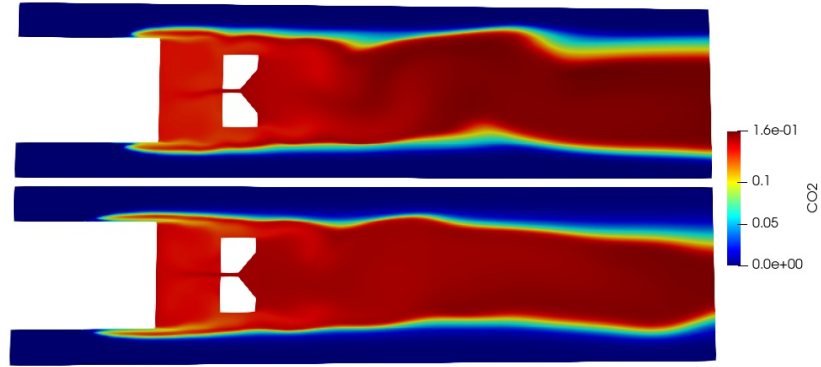


Figure 4.9: CO_2 distribution for $U_a = 75 \text{ m/s}$ (top) and $U = 25 \text{ m/s}$ (bottom)

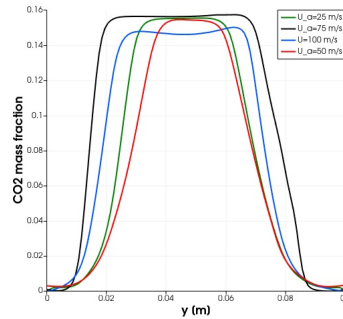


Figure 4.10: Outlet CO_2 mass fraction profile

4.1.4 CH_4 distribution and combustion efficiency

Besides pollutant emissions due to combustion process, *Flightpath 2050* objectives are also about fuel consumption and waste. This topic also concerns airway companies and aircraft manufacturers, in fact less fuel consumption means less fuel to purchase hence less costs and that is way it is very important to analyze and keep track of how much unburnt fuel exits the combustors doing the best to keep it to low levels.

The mass concentration for CH_4 almost immediately drops to half right after it enters the chamber which suggests that as soon as the fuel jets meet the fresh air from the horizontal jets, it is mixed with it. The values remains basically constant all the way to the external zones of the cavity and that explains those more yellow lines observed in fig.(4.8) and fig.(4.9). The amount of CH_4 lowers inside the cavity for it mixes with the fresh sucked in by the eddies. From fig.(4.12) one can see that for low U_a , more fuel is present within the eddies thus making the combustion process locally richer. For what concerns the flow after the second blunt bodies,



Figure 4.11: CH_4 distribution for $U_a = 50 \text{ m/s}$ (top) and $U = 100 \text{ m/s}$ (bottom)

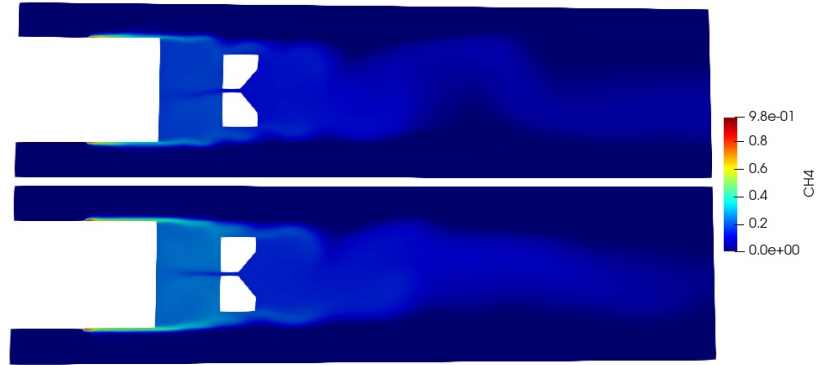


Figure 4.12: CH_4 distribution for $U_a = 75 \text{ m/s}$ (top) and $U = 25 \text{ m/s}$ (bottom)

for $U_a = 25 \text{ m/s}$, the eddies do not provide the sufficient pressure drop to suck in the fuel thus allowing a good portion of it to pass the first cavity and go to the second one as one can see from the more bright and longer areas around the blunt bodies. On the contrary but with similar results, for high air velocities, the CH_4 does not have enough residence time within the vortices, hence it is rejected outside of them before it can participate to the combustion. This deeply affects the amount of unburnt fuel at the outlet which in fact depends strongly on U_a as it is possible to see through the plot in fig.(4.13). In agreement with what has been said so far, the trend for the maximum amount of fuel mass fraction is not increasing monotone but a minimum point can be found. With the peak value, also the width of it increases with the velocity, probably due to the fact that most CH_4 does not enter the eddies but go past them and that contributes also to the fuel entering the eddies but does not stay for enough time for it to burn. It is important to say that the maximum peak value does not reach 0.09 which means that less than 9

% of the mass exiting the chamber is unburnt methane. This value can decrease or increase considering a more complex reaction mechanism with more than four elements and one reaction.

Another way to watch over fuel waste is combustion efficiency i.e. how much fuel

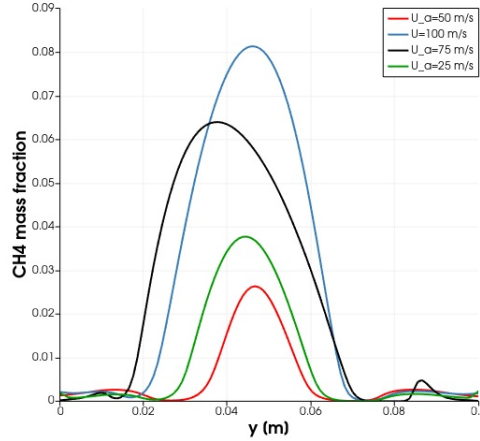


Figure 4.13: Efficiency trend with respect to air inlet velocity

exits the combustor with respect to how much is been fed at the inlet:

$$\eta_c = \frac{\dot{m}_{\text{CH}_4, \text{in}} - \dot{m}_{\text{CH}_4, \text{out}}}{\dot{m}_{\text{CH}_4, \text{in}}} \quad (4.1)$$

The calculation was done in terms of mass flow rather than masses per se for it was a bit easier getting mass flow data and keeping reliable values. In order to have a first order approximation value of it, a small Matlab script was written (all velocity, pressure, temperature, and mass fraction data were extrapolated through paraView tools):

```

1   MCO2=44.01; MO2=32; MCH4=16.04; MH2O=18.02; MN2=28.01; %molar
   masses
2   M_mis=(1./(YCO2/MCO2+YO2/MO2+YCH4/MCH4+YH2O/MH2O+YN2/MN2)); %
   mixture molar mass
3   m_dot_n_A=(P./(T*8314)).*M_mis.*U; %total mass flow for the n-th
   "cell" with respect to its Area
4   M_dot_n_A_i=m_dot_n_A.*YCH4; %stessa cosa di sopra ma solo del
   CH4
5
6   out = linspace(0,0.1,1001); %integration vector
7
8   m_dot_CH4_ex=trapz(out,M_dot_n_A_i)*0.1*0.1 %CH4 mass flow at the
   outlet

```

```

9
10 A_CH4=0.00059*0.1; %inlet Area [m^2]
11 U_CH4=37.5; %CH4 inlet velocity [m/s]
12 T_CH4=300; %CH4 inlet temperature [K]
13 P_CH4=104000; %CH4 inlet pressure [Pa]
14
15 m_dot_CH4_in=2*A_CH4*P_CH4/(T_CH4*8314)*U_CH4*MCH4 %CH4 inlet
mass flow
16
17 eff_4=(m_dot_CH4_in-m_dot_CH4_ex)/m_dot_CH4_in %efficiency

```

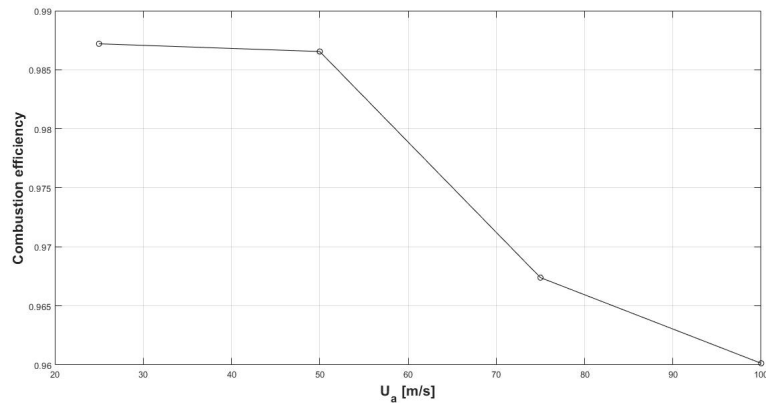


Figure 4.14: Efficiency trend with respect to air inlet velocity

The values obtained from this approximate calculation do not strain too much away from those in Zeng’s work [6] for $U_a = 50 \text{ m/s}$ and $\alpha = 60^\circ$ considering that this is a 2D simulation and the reaction mechanism is a lot simpler. What the plot in fig.(4.14) shows is the sudden drop in combustion efficiency when the air entering the chamber is higher than 50 m/s which and that may suggests that the working point for this type of combustor.

4.2 Penn State pre-burner

The purpose of the Penn State pre-burner study case is to understand if reacting-Foam is a valid CFD tool and for that the results obtained with this simulation are in a certain way compered (not explicitly) with the ones obtained in other studies[5] [8]. The thermodynamics characteristics of interest are obviously the development of the flow i.e. velocity distribution, Mach number, and streamlines. With those, temperature distribution, reaction product distribution i.e. H_2O as well as reactants. For all these flow properties plotted have been drowned with their values along a cross section right before the exit nozzle in order not to measure

values unaltered by the expansion in the nozzle. H_2 mass fraction values at the outlet section are important for they give some sort of measure of combustion efficiency (not calculated for this case). One thing needs to be said, in the x-axis of said plots, $x = 0.2 \text{ m}$ corresponds to the coordinate of the symmetry axis. Please note that the results of this case may deviate from the one in [5] [8] since a different and simpler reaction mechanism is used, anyway the results for main thermophysical properties are about the same. Finally, a close look on the flow evolution inside the nozzle is shown since it is what regulates the thermodynamics characteristics of the flow.

4.2.1 Fluid-dynamic

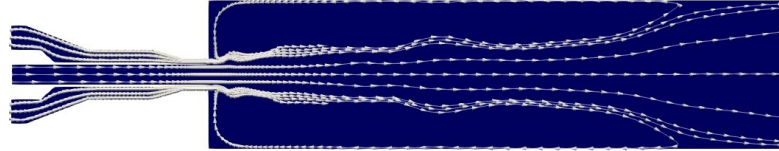


Figure 4.15: Streamlines highlighting outer eddie and main flow direction

The fluid-dynamic evolution of the flow it is axial-symmetric as one could have imagined as the pre-burner geometry is also axial-symmetric. As shown in fig.(4.17), the oxygen is fed into the main chamber with high velocities reaching almost Mach 0.6 and that, together with the mixing and combustion process result in some sort of lobe structures. Also the hydrogen enters the chamber at high velocities which are reached due to a strong reduction of its duct cross section (conservation of mass) as one can see from the more green colour of the flow in the narrower part of the inlet. It expands as soon as it exits the duct mixing immediately with the oxidizer. Past the transient phase, the flow seems to be characterized by two sub-flows: an inner flow which is made of 2 pairs of counter-rotating eddies which obviously may wiggle a bit during the pre-burner work(fig.(4.16)) and on outer flow which form a single pair of larger eddies and the core flow (fig.(4.15)). Both the inner and outer pairs of eddies help on keeping the flame burning oxygen and hydrogen. Besides the core of the chamber, the flow seems to be almost still in the outer zones of the combustor. The pressure in the chamber following the combustion matches the one obtained in the experimentation ($P \sim 5.6 \text{ MPa}$)

It may be interesting to focus on what happens at the outlet since the nozzle regulates the mass flow. As it is possible to see in fig.(4.18), the nozzle is choked

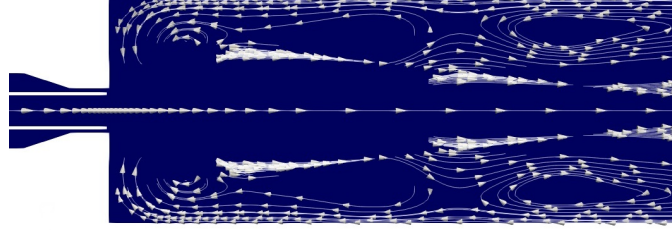


Figure 4.16: Streamlines highlighting eddies inside the chamber

in fact $Ma = 1$ at the throat and it reaches supersonic values at the outlet where $Ma \sim 2.9$. The streamlines highlight the ordered flow inside the nozzle without any sort of separation of the boundary layer. Fig.(4.19) shows the values for temperature, pressure, and Mach number along the symmetry axis within the nozzle to better visualize the evolution of the flow. As expected, both temperature and pressure drop following the flow expansion through the nozzle while the Mach increases. To be noted is the steep drop of the pressure localized where the throat is (z_0 in the bottom axis is the z coordinate where the line of measurement begins) while the temperature and the Mach have relative gentler gradients. In addition, the pressure at the exit of the nozzle matches the ambient pressure ($p_e = p_0$) which is set to 1 atm.

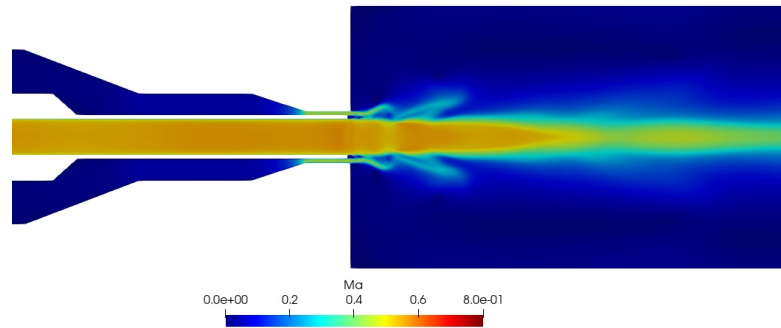


Figure 4.17: Mach number at the chamber inlet

4.2.2 Temperature distribution

The temperature profile obtained through reactingFoam resembles very well the one realized with experimental means. The maximum temperature reached with the combustion of hydrogen and oxygen (already in gaseous state) is obviously

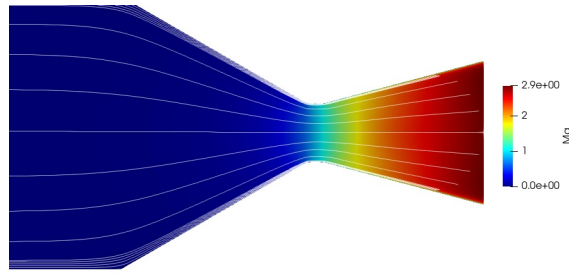


Figure 4.18: Mach number along the outlet nozzle

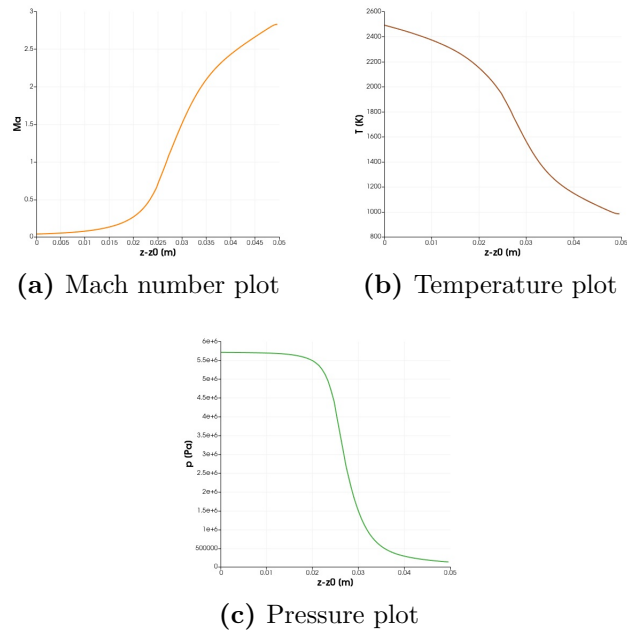


Figure 4.19: Measurements along the symmetry axis inside the outlet nozzle

higher with respect to methane and oxygen reaction due to hydrogen higher calorific value. This peak temperature matches the experimental one. From fig.(4.20) two main zones can be noted i.e. the one right outside the injector and the rest of the chamber (the nozzle has already been discussed). The temperature distribution in the first zone is affected by the injection of fuel and oxidizer, in fact one can see that here the hydrogen temperature is still relevant while the oxygen is the main player in that region. Here, H_2 and O_2 mix and the combustion process starts as the more red area shows. The remainder of the combustion chamber sees a core zone occupied by "cold" oxygen which high velocities push it far into the chamber. The hot flame is right at the border of the unburnt oxygen and it comes back towards

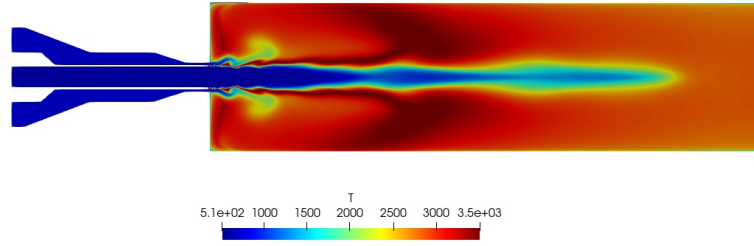


Figure 4.20: Temperature profile

the injector through the eddies seen in the previous subsection. The oxygen also works as refrigerant cooling to $T \sim 3000\text{ K}$ the temperature inside the chamber. The plot in fig.(4.21) shows that the hot gas (H_2O) product of the combustion is not just focused in a narrow region around the symmetry axis but is spread across the entire chamber. It is possible to see the temperature boundary layer at the extremity of the chamber close the walls.

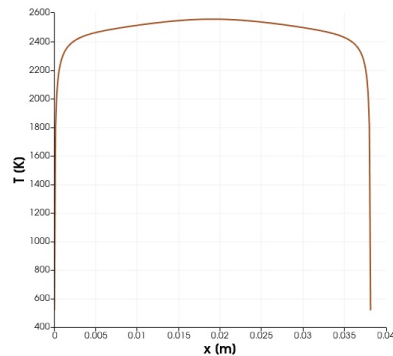


Figure 4.21: Temperature measurements for a cross section at $z = 0.285\text{ m}$

4.2.3 H_2O , N_2 , and O_2 distribution

Just like the CO_2 in the AVC, the distribution of H_2O in the combustion chamber resembles the temperature distribution since the major cause of it is the reaction product, in this case just water. First thing to be noted is that yellow colour in the hydrogen part of the injector but that normal since the composition of fuel is 40 % hydrogen and 60 % water in fact that colour corresponds to a 0.6 mass fraction. For the first part of the chamber, H_2O is basically one to one with temperature, its presence starts right outside the injector where fuel and oxidizer

mix and react with one another, than it seems that the inner and outer eddies keep the majority of the water close to the injector which may be a positive aspect since its temperature helps sustain the combustion process heating the reactants to the right temperatures.

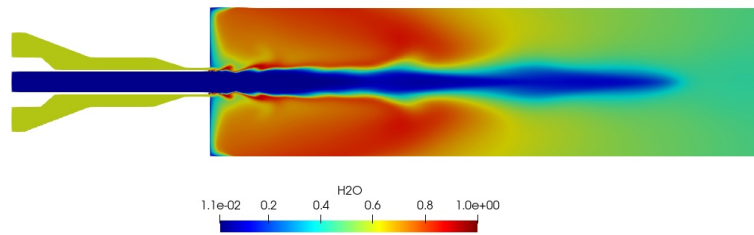


Figure 4.22: H₂O distribution in the chamber

One can notice a green and bluer area next to "vertical" wall of the chamber which indicates minor presence of combustion product and that is due to N₂ as shown in fig.(4.23). In this case, keeping track of the N₂ mass fraction is important in order to understand how far gone is the combustion since the nitrogen is the only element the was present in the beginning of the simulation. It is noticeable that just a very small part of it is kept inside that chamber due to the vortices. In

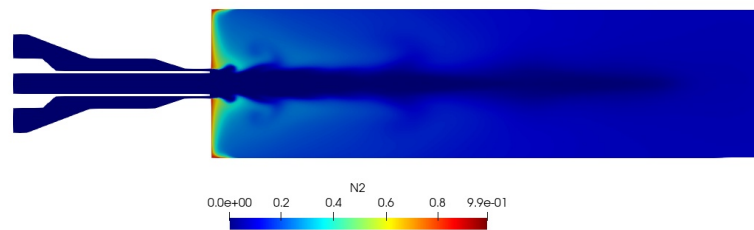


Figure 4.23: N₂ distribution inside the chamber

fig.(4.22) one can see that going further into the chamber, less and less water is present, in fact it is replaced in some parts by the oxygen which was "crashed" into the centre of the chamber by the eddies previously but later it is free to occupy the whole height of the combustor and this phenomenon is visible in fig.(4.24) where initially blue colour is dominant in the aft part but later a greener area is spotted

indicating the more amount of oxygen. This oxygen is heated by the H_2O and it becomes the main reason for the high temperatures. For the sake of completeness,

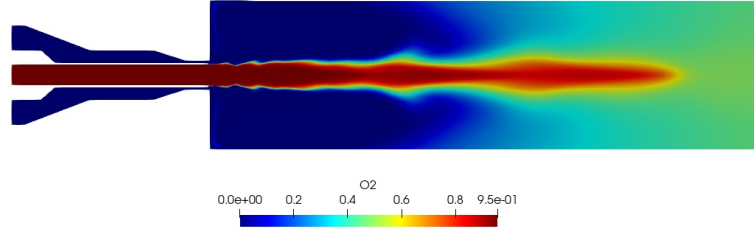


Figure 4.24: O_2 distribution inside the chamber

in fig.(4.25) the measurements of these mass fractions at the chamber outlet are shown. The first thing that pops up is that as the H_2O quantity goes down, the mass fractions of N_2 and O_2 raise. This happens as the water is mostly kept in the first part of the chamber by the eddies and it is forced in the outer areas near the walls, hence the peaks in the right and left side of the plot. A point of maximum is present in correspondence of the symmetry axis, probably due to the flow sucking in back from the outside the water and rejecting N_2 and O_2 . Even though the values of nitrogen are relevant, it is easy to say that the flow exiting the chamber is made up mostly of unburnt oxygen, one and half times more than water and almost four times more than nitrogen. Both N_2 and O_2 have points of relative minimum where H_2O has its maximum.

4.2.4 H_2 distribution

Keeping track of H_2 presence inside the chamber helps understand how efficient the combustion process is and accordingly how much fuel waste is produced. Fig.(4.26) does a tremendous job showing how much hydrogen "survives" the combustion which is basically none in fact one can see that the most amount of H_2 is localized right outside the injector where the mass fraction quickly halves from 0.4 to around 0.2. After that, the 2 symmetrical eddies in the first part recirculate the hydrogen keeping it from going towards the exit. This gives the hydrogen that did not burn a second chance to participate to the reaction which eventually does in fact the second part of the chamber is characterized by a dark blue colour which stands for hydrogen absence.

In order to further state the combustion efficiency, as done for the other species, measurements of H_2 mass fraction at the chamber outlet right before the nozzle

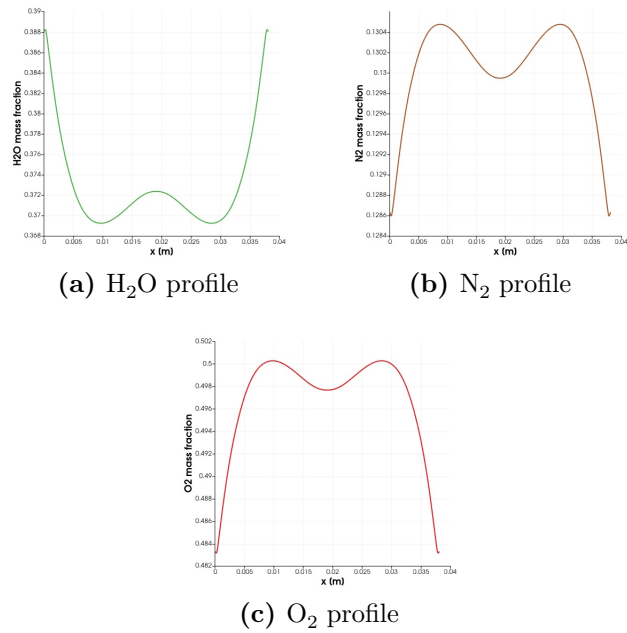


Figure 4.25: H₂O, N₂, and O₂ mass fraction measurements for a cross section at $z = 0.285 \text{ m}$

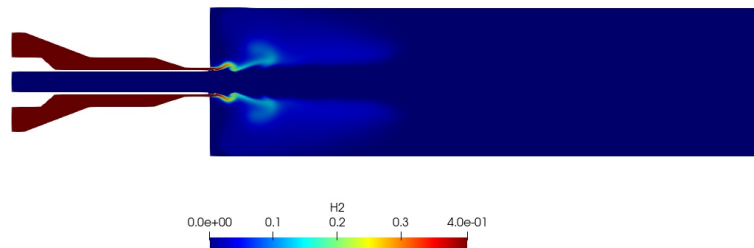


Figure 4.26: H₂O distribution in the chamber

were taken. What stands out first of all is the mass fraction values which go from 10^{-5} to 10^{-6} . These are very low numbers indicating that basically no hydrogen reaches the nozzle thus indicating a very efficient combustion process with no fuel waste at all.

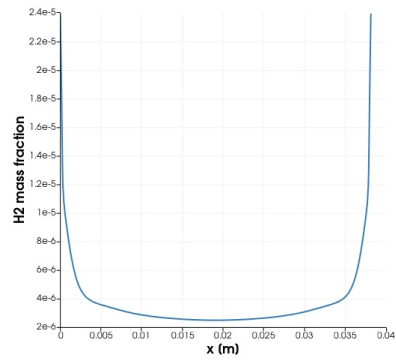


Figure 4.27: H₂ mass fraction measurements for a cross section put at $z = 0.285$ m

Chapter 5

Conclusions

This work had two main objectives: simulate a combustion in an advanced combustor i.e. not a standard ring combustor, and to study the potential of an open source software like openFOAM in simulating this kind of reacting flows. To fulfill those objectives, first of all a brief overview was made of those thermophysical laws that regulates the behavior of fluids and their reaction if it is the case of chemically reacting flows. After that, numerical means for how those laws are solved have been introduced, together with main schemes used in Computational Fluid-dynamics (CFD). Next the study cases have been presented with all settings concerning numerical schemes and geometry. It is important to understand that the simulation done in this work are not a work of refinement but they should be considered as a first approximation in order to have an idea where to work to perfect a certain reaction mechanism or geometrical layout. Said so, the simulation of methane and air combustion in the advanced trapped vortex showed promising results for possible application whether in classic turbofan jet engines or for RAMjet installed in high supersonic aircrafts. For these last application, the combustor showed a significant, but not too much, decrease in combustion efficiency i.e. how much unburnt fuel exits the combustor suggesting modification in the geometry for this kind of working condition. High velocities did not interfere in gaining high temperatures which mean high amount of work that can be extrapolated by the turbine following the combustor (if it installed in a classic jet engine). Also levels of CO_2 and N_2 were tracked. For what concern the Penn State case, a single set of boundary condition was studied emulating as good as possible the experimental setups used in previous work [5] [8]. The results gather for this case show a maximum flame temperature of about 3500 K against the 2500 K for the AVC case but that was expected since H_2 has higher heating power than methane does. The nozzle is choked which is an example of the perfect condition at which the pre-burner works. A fundamental results that stands out is the incredibly low level of hydrogen mass fraction which indicates a efficient combustion with no fuel

waste whatsoever. The pressure inside the chamber matches the one obtained during the experimentation with some small deviation but still acceptable.

For both test case, one step reaction method were used obtaining results that give an idea of what is the actual combustion process inside each type of combustor. In order to have a more complete picture of the behavior of reacting flows inside them, further work should focus on applying more complex reaction mechanisms which could not be done in this work due to limit amount of time. For the AVC case, it would be interesting to use this software to analyze NO_x and CO for different working conditions.

Finally, these cases proved the adaptability and capability of reactingFoam in simulating different type of reactant in different type of geometry and boundary conditions. Still, some work needs to be done in order to find the best setup possible to reach numerical convergence with more than one reaction the quickest.

Bibliography

- [1] Group of personalities. *European Aeronautics: a vision for 2020*. European Commission, 2021 (cit. on p. 1).
- [2] Directorate-General for Research, Directorate-General for Mobility Innovation, and Transport. *Flightpath 2050 Europe’s Vision for Aviation*. European Commission, 2011 (cit. on p. 1).
- [3] Dan Zhao, Ephraim Gutmark, and Philip de Goey. “A review of cavity-based trapped vortex, ultra-compact, high-g, inter-turbine combustors”. eng. In: *Progress in energy and combustion science* 66 (2018), pp. 42–82. ISSN: 0360-1285 (cit. on p. 2).
- [4] Dominik Christ. *Simulating the combustion of gaseous fuels*. during the 6th OpenFOAM Workshop. 2012. URL: https://openfoamwiki.net/images/8/8a/Christ_0FW6_slides.pdf (cit. on pp. 25, 26).
- [5] Marco Invigorito, Daniele Cardillo, and Giuliano Ranuzzi. “Application of OpenFOAM for Rocket Design”. In: June 2014 (cit. on pp. 48, 66, 67, 75).
- [6] Zhuoxiong Zeng, Peng Du, Zhikai Wang, and Kai Li. “Combustion flow in different advanced vortex combustors with/without vortex generator”. In: *Aerospace Science and Technology* 86 (2019), pp. 640–649. ISSN: 1270-9638 (cit. on pp. 48, 50, 57, 66).
- [7] Federico Municchi, Pranay Nagrani, and Ivan Christov. *A two-fluid model for numerical simulation of shear-dominated suspension flows*. Nov. 2018 (cit. on p. 51).
- [8] KB Koshelev and SV Strijhak. “Application of reactingCentralFOAM for modeling processes in combustion test chamber”. In: *AIP Conference Proceedings*. Vol. 2027. 1. AIP Publishing LLC. 2018, p. 030093 (cit. on pp. 53–55, 66, 67, 75).

- [9] Michael P. Burke, Marcos Chaos, Yiguang Ju, Frederick L. Dryer, and Stephen J. Klippenstein. “Comprehensive H₂/O₂ kinetic model for high-pressure combustion”. In: *International Journal of Chemical Kinetics* 44.7 (2012), pp. 444–474. DOI: <https://doi.org/10.1002/kin.20603>. eprint: <https://onlinelibrary.wiley.com/doi/pdf/10.1002/kin.20603>. URL: <https://onlinelibrary.wiley.com/doi/abs/10.1002/kin.20603> (cit. on p. 54).

Acknowledgements

Chi mi conosce sa che sono una persona riservata e di poche parole ma credo che questa occasione meriti un certo sforzo nel dire qualche parolina. Questi duri anni passati al Politecnico sono stati pieni di ansia pre-esami, disperazione per progetti e studio a non finire. Non ce l'avrei certamente fatta senza delle persone al mio fianco, senza qualcuno che credesse sempre in me anche quando io stentavo a farlo e che rendesse questi anni un cammino meraviglioso. Vorrei dunque usare questa pagina per ringraziarle di tutto.

Prima di tutto vorrei ringraziare il mio relatore, il professore M. Ferlauto il quale mi ha assistito instancabilmente durante questo percorso durato parecchi mesi fornendomi tutto il materiale necessario, consigli e una chiara guida per il mio lavoro.

Un immenso grazie va alla mia famiglia: a papà che mi ha trasmesso la passione per l'aeronautica, a mamma sempre in ascolto ogni sera durante il solito minuto al telefono con papà, a Giuseppe con il quale condivido l'amore per l'aviazione, a Chiara e alle domeniche passate a mangiare ragù, risotto e pasta sfoglia, a Fabio, fratello, amico e ingegnere. Zie, zii, cugini e cugine, Cindy, Barry, e Doug.

Grazie ai miei compagni di avventura: Ale, Guido, Luca, Leo, Masca, Marina e Rai i quali hanno sopportato le mie quotidiane lamentele, *falzità*, condiviso momenti di ansia e gioia e, soprattutto, mi hanno sostenuto in questi ultimi davvero difficili. A proposito vorrei ringraziare particolarmente Leo e l'Avvocato i quali hanno fatto sì che la mia testa tornasse sempre al suo posto quando questa vagava tra le nuvole.

Ringrazio Francesco con cui ho condiviso le emozioni dei primi esami, Andrea e i sabato pomeriggio passati alla Comunale di Torino a perdere la voce e l'udito.

Per ultimo ma certamente non per importanza, tutti i miei amici di sempre senza quale supporto sicuramente non sarei arrivato fin qua.

Ancora un sentito grazie a tutti.

Salvatore Manganaro

Torino, 24 Marzo 2021.